nature genetics

Article

https://doi.org/10.1038/s41588-026-02615-w

Spatially resolved single-cell analyses of human meningioma identify novel cell states influencing tumor microenvironment and progression

Received: 17 July 2025

Accepted: 28 April 2026

Published online: 09 June 2026

Check for updates

Alexander P. Landry[1,2,3], Leeor S. Yefet[1,2,3], Justin Z. Wang[1,2,3], Andrew Ajisebutu[1,3], Chloe Gui[1,2,3], Yosef Ellenbogen[1,2,3], Jeff Liu[1,3], Vikas Patil[1,3], Colleen Q. Ding[1,3], Qingxia Wei[1,3], Sheila Mansouri[1,3,4], Olivia Singh[1,3,4], Aaron A. Cohen-Gadol[5,6], Derek S. Tsang[7], Andrew Gao[8], Kenneth Aldape[9], Farshad Nassiri[1,2,3] ✉ & Gelareh Zadeh[1,2,3,4] ✉

Recent advances in our understanding of the molecular landscape of meningioma have generated new insights into the biology and heterogeneity of this disease, with demonstrated clinical value. However, there remains a need to understand tumor-intrinsic heterogeneity at single-cell resolution to inform potential therapeutic avenues. In this study, we examined the breadth of cell types and states in meningioma using a large cohort profiled with single-nuclear RNA sequencing and high-resolution spatial transcriptomics, as well as bulk DNA methylation and RNA sequencing ($n = 712$), bulk proteomics ($n = 88$) and plasma methylation ($n = 59$). We demonstrated that myeloid cell states differ across molecular groups of meningiomas and evolve meaningfully from dura to tumor. Myeloid cell states were also associated with unique myeloid–neoplastic interactions and neoplastic gene programs, suggesting a role in shaping the microenvironment. Finally, multiple non-neoplastic cell states refined outcome prediction beyond molecular group, suggesting a role in meningioma progression.

Meningioma represents the most common brain tumor in adults[1] and is associated with profound clinical heterogeneity that is not fully captured by World Health Organization (WHO) grading. This has led to the development of molecular taxonomies that can more robustly predict clinical behavior[2–14]. We previously established four molecular groups (MGs) of meningioma: immunogenic (MG1), with immune infiltration and favorable outcomes; NF2-wildtype (MG2), with non-NF2 driver mutations and favorable outcomes; hypermetabolic (MG3), with upregulated metabolism pathways and intermediate to poor outcomes; and proliferative (MG4), with cell-cycle activation, poor outcomes and resistance to radiotherapy[4,6,8]. Other research groups have independently reinforced the value of molecular classification in meningioma[12,13,15]. Additionally, cytogenetic alterations (particularly loss of chromosomes 22q and 1p) have recently been highlighted as a potential adjunct to WHO grading for meningioma[7,9], although the sensitivity of these alterations to regional sampling bias remains unclear.

[1]MacFeeters Hamilton Neuro-Oncology Program, Princess Margaret Cancer Centre, University Health Network and University of Toronto, Toronto, Ontario, Canada. [2]Division of Neurosurgery, Department of Surgery, University of Toronto, Toronto, Ontario, Canada. [3]Princess Margaret Cancer Centre, University Health Network, Toronto, Ontario, Canada. [4]Department of Neurologic Surgery, Mayo Clinic, Rochester, MN, USA. [5]ATLAS Institute of Brain and Spine, Los Angeles, CA, USA. [6]University of Utah Health, Salt Lake City, UT, USA. [7]Radiation Medicine Program, Princess Margaret Cancer Centre, Toronto, Ontario, Canada. [8]Laboratory Medicine Program, University Health Network, Toronto, Ontario, Canada. [9]Department of Laboratory Medicine and Pathology, Mayo Clinic, Rochester, MN, USA. ✉e-mail: farshad.nassiri@uhn.ca; zadeh.gelareh@mayo.edu

Building on these discoveries and studies from other cancers demonstrating the profound importance of the microenvironment[16–19], an important next step in meningioma research is to resolve tumor-level heterogeneity using single-cell and spatially resolved genomics. To accomplish this goal, we generated a large cohort of meningioma single-nuclear RNA sequencing (snRNA-seq) and spatial transcriptomics, including regional sampling from the tumor and surrounding dura. This allowed for deep characterization of the cell types and states constituting the meningioma microenvironment, leading to insights into the role of both neoplastic and non-neoplastic cells in meningioma biology and outcome.

Results

Study cohort

Our cohort focused on snRNA-seq (n = 102 samples and 580,185 high-quality nuclei) and spatial transcriptomics (Visium HD, n = 43 samples and 7,146,538 segmented cells). Bulk DNA methylation was used to classify cases by MG using our published model[6]. Paired bulk DNA methylation and RNA-seq was used to validate results from the single-cell resolution data and interrogate their influence on clinical outcomes. These bulk samples were obtained from University Health Network (Toronto), Indiana University, Case Western University, the Fred Hutchison Cancer Center, the RTOG-0539 clinical trial and publicly available datasets[12,13] (n = 712; Fig. 1a). We also performed shotgun proteomics (n = 88) and plasma methylation sequencing[20–22] (n = 59) on a subset of cases.

A single-cell atlas of meningioma reveals recurrent transcriptional metaprograms

To understand the transcriptional diversity of meningioma cell populations, we first defined an 'atlas' cohort from our snRNA-seq data (n = 68 samples; 392,818 high-quality nuclei). Most cells were neoplastic (74.9%, n = 294,122), and myeloid cells dominated the non-neoplastic compartment (22.3% of all cells, n = 87,482). Lymphoid (1.5%, n = 5,778) and endothelial cells (n = 1.4%, 5,436) were comparatively rare (Fig. 1b and Extended Data Fig. 1). Non-negative matrix factorization (NMF) was used to identify recurrent transcriptional programs (metaprograms (MPs)) within each cell type. Among neoplastic cells, 11 MPs were identified, although only two (MP1 and MP11) were consistently shared across most samples, probably owing to known inter-individual variation of meningioma neoplastic cells[4] (Fig. 1c and Supplementary Figs. 1a and 2). These highly shared MPs were defined by cell-cycle genes (cycling) and metabolic or ribosomal genes (metabolic), respectively. Other neoplastic MPs were identified only within smaller subsets of samples, suggesting considerable transcriptional diversity between neoplastic cell populations of different tumors, such that only a subset of transcriptional programs is shared across most cases. Of these rarer neoplastic MPs, some were defined by clear biological processes (interferon (IFN)-related pathways (MP3), tumor necrosis factor (TNF)-related pathways (MP5), epithelial-to-mesenchymal transition (EMT)-related pathways (MP6, MP9 and MP10) and inflammation-related pathways (MP7)). Others did not clearly map to a consistent biological function (MP2, MP4 and MP8).

Among non-neoplastic cells, seven myeloid MPs were identified. One was uniquely expressed in mast cells (representing <0.5% of myeloid cells). The remaining six were defined by (1) cell-cycle pathways (cycling); (2) IFN-related pathways (IFN/surveillance); (3) mixed pathway activation, with some specificity toward the EMT; (4) inflammatory or TNF-associated pathways (TNF/inflammatory); (5) tissue-repair-related pathways, including IL-6 and JAK–STAT (tissue repair); and (6) ribosomal and oxidative-phosphorylation-associated genes (metabolic) (Fig. 1d). Similarly, six lymphoid MPs (metabolic, cycling, IL-2, naive T cells, B cells and natural killer cells; Supplementary Fig. 1b) and four endothelial MPs (metabolic, TNF/hypoxia, complement and extracellular matrix (ECM)/EMT; Supplementary Fig. 1c) were identified. No MPs appeared to be driven by ambient RNA contamination, although one rare neoplastic MP (MP7) and one lymphoid MP (B cells) had a median ambient RNA content of >0.2 (Supplementary Fig. 3). Given that this lymphoid MP was clearly associated with a well-defined cell type, it was felt that removing cells based on inferred ambient RNA content risked removing meaningful biological signal.

We orthogonally validated these MPs using unsupervised clustering and by applying NMF to publicly available single-cell RNA cohorts of meningioma[23–25], demonstrating an absence of meaningful new transcriptional MPs and highlighting that large cohorts are needed to identify rarer MPs such as the myeloid EMT and lymphoid B cell MPs (Supplementary Note, Supplementary Fig. 4 and Extended Data Fig. 2). We also found that the cycling state (based on highest expressed MP) was associated with the highest inferred developmental potential across cell types and that neoplastic states were generally associated with higher developmental potential than non-neoplastic states (Supplementary Note and Supplementary Fig. 5).

Comparing MPs across cell types based on shared MP-defining genes, we found the metabolic MPs to be most similar across all cell types, with the cycling MPs also similar between the myeloid, neoplastic and lymphoid cells (details in Supplemental Note). A subset of other neoplastic MPs also shared genes with myeloid MPs (IFN-like, EMT-like, TNF-like; Fig. 1e and Supplementary Fig. 1d). Similar findings were demonstrated by comparing MP expression across cell types (Supplementary Fig. 6a), wherein some MPs exhibited similar expression across cell types (that is, metabolic and cycling), while others were specific to one cell type (that is, the myeloid tissue repair MP).

Myeloid cell states are differentially enriched across existing biological classifications

Given that myeloid cells represent most non-neoplastic cells within meningioma and are not associated with the same degree of inter-tumoral heterogeneity as are neoplastic cells, we focused on further characterizing their MPs within the context of known meningioma biology (Fig. 1f). Specifically, we sought to understand whether meningioma MGs were associated with differences in not only the abundance (as previously demonstrated[4]), but also the transcriptional profiles of constituent myeloid cells. To do so, myeloid cell-specific gene expression was averaged across each tumor (pseudobulk data,

Fig. 1 | The meningioma microenvironment exhibits considerable transcriptional diversity and can be defined by recurrent cell-type-specific metaprogams. a, Graphical depiction of study cohort. Created in BioRender; Singh, O. https://BioRender.com/98ou2xy (2026). **b**, Uniform manifold approximation and projection (UMAP) representation of our 'atlas' cohort of 68 patients with meningioma, with color representing cell type. **c**, Heatmap of filtered neoplastic programs, clustered by Jaccard index (left). The two dominant MPs are labeled based on constituent overlapping genes. UMAP of neoplastic cells, with cell state assigned based on the highest expressed MP (right). The dominant MPs (cycling and metabolic) are labeled. **d**, Heatmap of filtered myeloid programs, clustered by Jaccard index (left). UMAP of cells, with cell state assigned based on the highest expressed MP (right). Tis. rep., tissue repair. **e**, Heatmap depicting similarity between myeloid (rows) and neoplastic (columns) MPs. Color is by Jaccard index of MP-defining gene lists for each comparison. **f**, Expression of each MP across each myeloid cell in the atlas cohort. Expr., expression. **g**, Pseudobulk expression of the cycling, EMT, TFN and tissue repair myeloid MPs stratified by MG (n = 11 MG1, 17 MG2, 17 MG3, 16 MG4). Boxplot center lines represent the median, with the box spanning the interquartile range (25th–75th percentile); whiskers extend to the most extreme values within 1.5 times the interquartile range from the quartiles. **h**, Pie chart depicting the relative proportion of each cell state across all myeloid cells in our atlas cohort (left). Stacked barplots depicting the relative proportions of each myeloid cell state stratified by MG (right).

https://doi.org/10.1038/s41588-026-02615-w

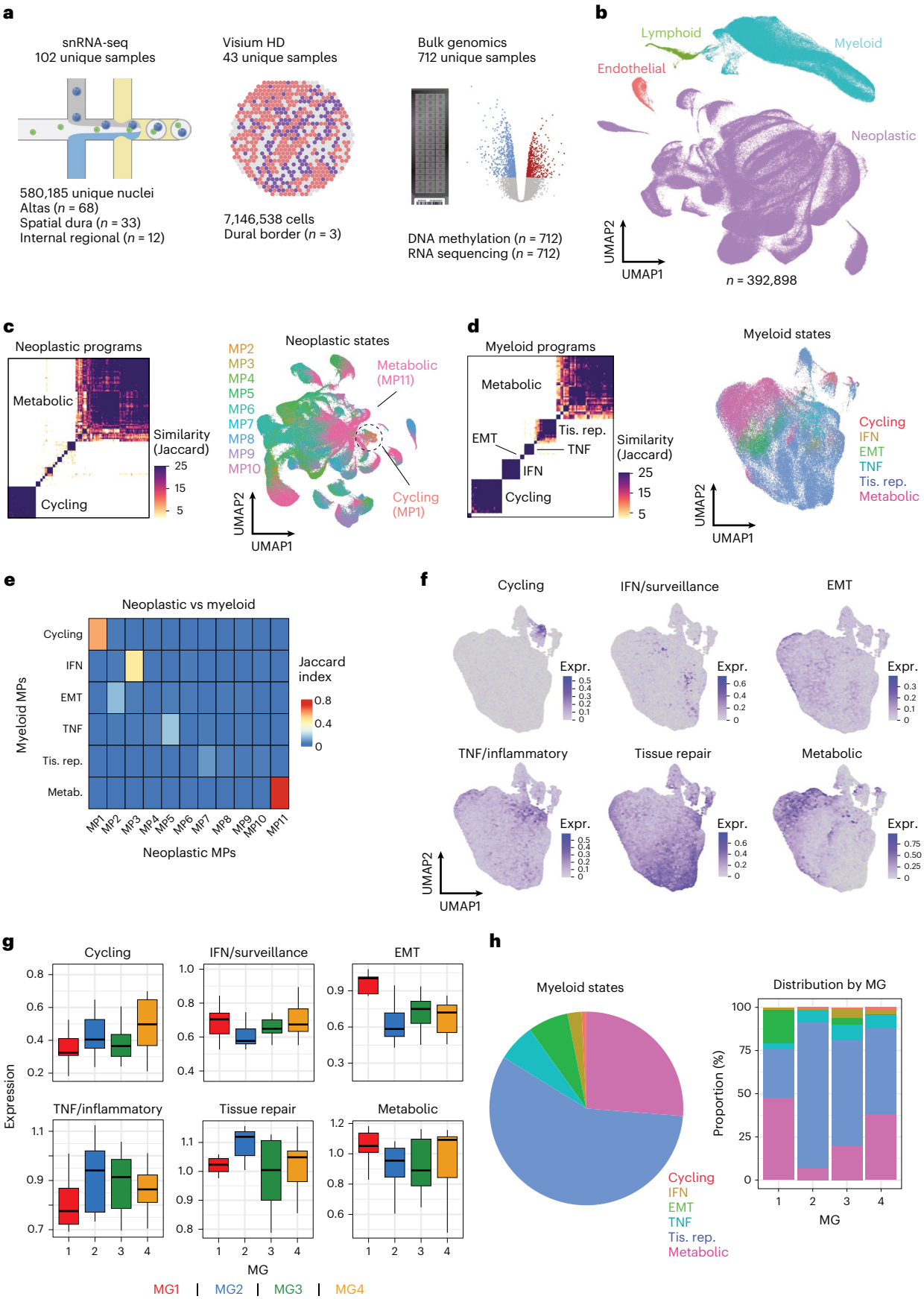

https://doi.org/10.1038/s41588-026-02615-w

to allow per-sample comparisons) and myeloid MPs quantified using single-sample gene set enrichment analysis (ssGSEA). The cycling MP was upregulated in proliferative cases (Wilcox $P = 0.03$), the EMT MP was upregulated in immunogenic cases (Wilcox $P = 1.5 \times 10^{-5}$), the TNF MP was downregulated in immunogenic cases (Wilcox $P = 0.02$) and the tissue repair MP was upregulated in NF2-wildtype cases (Wilcox $P = 1.3 \times 10^{-4}$) (Fig. 1g). The cycling MP also significantly increased with WHO grade (ANOVA $P = 2.5 \times 10^{-4}$), while the tissue repair MP was significantly upregulated in WHO grade 1 cases compared to WHO grade 2 or 3 cases (Wilcox $P = 0.004$; Supplementary Fig. 6b).

Comparing myeloid cell states between MGs, we found that tissue repair cells were most abundant overall ($n = 50{,}374$; 57.6%) and particularly common in MG2 ($n = 20{,}493$ out of 24,194 (84.7%), chi-squared $P < 2.2 \times 10^{-16}$ MG2 vs others). However, they were least common in MG1 ($n = 7{,}251$ out of 25,456 (29.5%), $P < 2.2 \times 10^{-16}$ MG1 vs others). Metabolic myeloid cells were next most common ($n = 22{,}962$; 26.2% overall) and were least frequent in MG2 ($n = 1{,}585$ (6.6%), $P < 2.2 \times 10^{-16}$ MG2 vs others). There were 5,890 EMT myeloid cells (6.7%) that were most common in MG1 meningiomas (4,954 out of 25,456 (19.4%), $P < 2.2 \times 10^{-16}$ MG1 vs others), whereas TNF myeloid cells were least common in MG1 ($n = 792$ (3.1%), $P < 2.2 \times 10^{-16}$ MG1 vs others). Cycling myeloid cells were rare overall, in keeping with prior literature[26] ($n = 685$; 0.8%), but were enriched in MG3 and MG4 ($n = 439$ out of 34,539 (1.3%)) compared to MG1 and MG2 ($P < 2.2 \times 10^{-16}$) (Fig. 1h). These findings were validated with bulk deconvolution (Supplementary Note and Supplementary Fig. 7). Overall, we demonstrate that myeloid cells take on biological signatures that correlate with overall tumor biology, as reflected by MG and WHO grade, suggesting their important role within meningioma biology and potential influence on clinical outcomes.

Some myeloid MPs are consistent with myeloid gene programs from glioblastoma

To investigate whether myeloid MPs are meningioma-specific, we compared them to analogous gene programs identified in glioblastoma (GBM)[16], identifying strong correlations with the cycling, IFN and TNF MPs and moderate correlations with the tissue repair and metabolic MPs; no GBM programs corresponded to the EMT MP (Supplementary Fig. 8 and Supplementary Note). This finding suggests that many myeloid transcriptional programs are conserved across GBM and meningioma to various degrees, adding additional context to our results.

Bulk proteomic analysis validates the biological correlates of myeloid MPs

We next used our bulk proteomics cohort to orthogonally validate the biology of each myeloid MP and identify candidate markers (details in Supplementary Note). Proteomic pathways largely corresponded with the RNA-based pathways associated with each MP[27] (Supplementary Fig. 9). LMNB1 was found to be the best marker for the cycling myeloid MP; STAT1 for the IFN MP, NFIA for the EMT MP, SLC2A3 for the TNF MP, MRC1for the tissue repair MP and PHPT1 for the metabolic MP (Extended Data Fig. 3). Notably, specificity was imperfect, suggesting that single marker genes or proteins may not be as reliable as multi-gene signatures to identify these complex and overlapping myeloid cell states.

Some meningiomas exhibit considerable neoplastic transcriptional heterogeneity over space

Given the finding that the myeloid cells varied based on WHO grade and MG, we next sought to explore whether these myeloid MPs, in addition to neoplastic MPs, also vary across different physical regions of the same tumor. To do so, we leveraged a dedicated 'internal regional' cohort consisting of three regionally distinct samples from four meningiomas with snRNA-seq and bulk methylation profiling ($n = 12$ samples and 110,318 cells; Fig. 2a,b, Supplementary Fig. 10 and Supplementary Note).

To quantify the degree of per-sample transcriptional variance in the context of our established MPs, ANOVA was used to compare the expression of each MP between samples (Supplementary Fig. 11). The average F-statistic across all MPs (F_{avg}) was used to represent the overall regionally driven transcriptional variation for a particular tumor. Differences in F_{avg} among myeloid cells were not statistically significant (Fig. 2c), but among the neoplastic cells, one sample (P3) was associated with significantly higher heterogeneity than the others (Fig. 2d and Supplementary Note). These findings, although limited to a cohort of four meningiomas, suggest that neoplastic cells may exhibit considerable transcriptional variation across different regions, whereas myeloid populations do not appear to exhibit the same degree of regional heterogeneity.

Neoplastic chromosome 1p and 22q losses are largely stable across whole meningiomas

The identification of regional neoplastic heterogeneity in some meningioma samples could suggest spatial differences in chromosomal copy number alterations, which could have important implications if used as biomarkers. Specifically, this would indicate a need for multi-regional sampling in the clinical setting, which is not currently done. Given their increasingly established role as meningioma biomarkers, we compared the proportion of neoplastic cells with chromosome 22q and 1p losses over distinct regions[7,9]. Reassuringly, we found similar proportions among samples from the same patient, and importantly, all samples from P3 (associated with marked transcriptional heterogeneity) had

Fig. 2 | Regionally diverse sampling within the same meningiomas identifies transcriptional intra-tumoral heterogeneity but comparatively stable copy number alterations. a, Example representative axial T1-weighted magnetic resonance imaging with gadolinium contrast of one patient in our internal regional cohort, with multiple stereotactically registered samples obtained from the same tumor. **b**, UMAP plot annotated by cell type. **c**, UMAP representation of myeloid cells in this cohort, annotated by sample of origin (left (P, patient; T, tumor)). Boxplot (and superimposed jitter plot) depicting F-statistic of myeloid MPs by patient (right, $n = 6$ MPs each). **d**, UMAP representation of neoplastic cells in this cohort, annotated by sample of origin (left). Boxplot depicting F-statistic of neoplastic MPs by patient (right, $n = 11$ MPs each). Example boxplots associated with the highest F-statistic in P3 ($n = 1{,}255$ cells for T1; 15,138 cells for T2; 11,717 cells for T3) and P1 ($n = 2{,}911$ cells for T1; 852 cells for T2; 1,789 cells for T3) are inset. **e**, Density plots of chromosome 1p and 22q deviations for all neoplastic cells from each individual patient (black lines) compared to normal dura reference (green lines), identifying −0.8 as an appropriate threshold to define a loss (top). Scatterplot depicting the proportion of cells from each sample with chromosome 1p or 22q losses based on this threshold, labeled by patient (bottom). Chr., chromosome. **f**, Scatterplot depicting $\log_2$(copy number variation, CNV) values for chromosome 1p and 22q from bulk DNA methylation (top) and boxplot of methylome risk scores by patient (bottom; $n = 5$ from P1, 5 from P2, 6 from P3, 3 from P4). **g**, Boxplots depicting inferred proportion of cells with chromosome 1p or 22q loss by snRNA, stratified by predicted CNV status by methylation on the full atlas cohort ($n = 28$ 1p loss, 34 neutral; $n = 61$ 22q loss, 21 neutral). Examples of discordance are plotted, with possible (albeit rare) cases of clonal heterogeneity highlighted (*). **h**, Analysis of local neoplastic transcriptomic heterogeneity using our spatial transcriptomic cohort. Example case of a meningioma with low spatial heterogeneity (indicated by low Moran's index) in one neoplastic MP (MP10) and high spatial heterogeneity in another neoplastic MP from the same sample (MP5; top). Grouped boxplots of per-sample Moran's indices within each neoplastic MP, stratified by the presence of a chromosome 1p loss (top boxplot; $n = 20$ loss, 23 neutral) or a chromosome 22q loss (bottom boxplot; $n = 34$ loss, 9 neutral). For all boxplots in this figure, center lines represent the median and the box spans the interquartile range (25^{th}–75^{th} percentile); whiskers extend to the most extreme values within 1.5 times the interquartile range beyond the quartiles.

https://doi.org/10.1038/s41588-026-02615-w

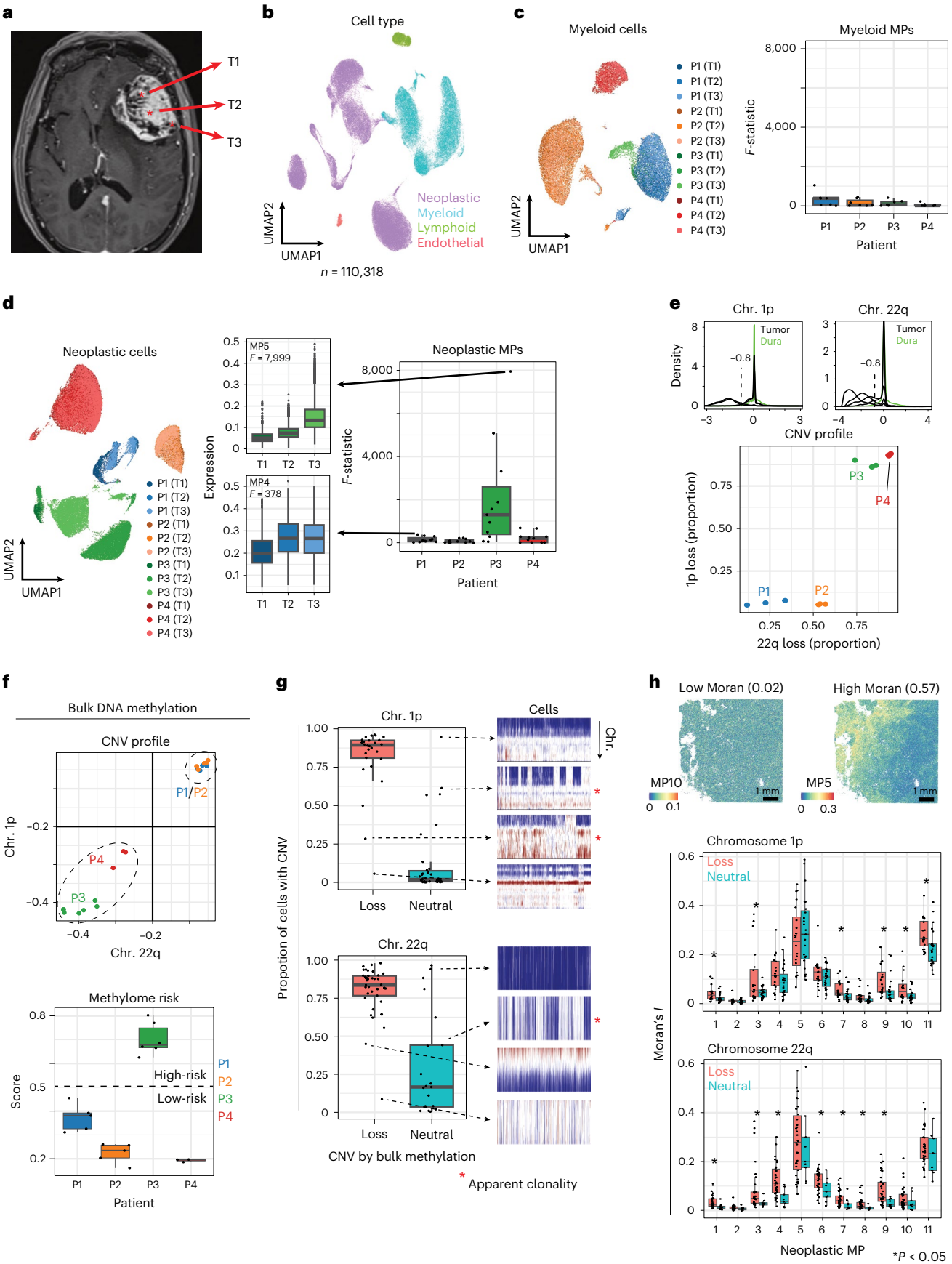

similar proportions of chromosome 1p loss (0.90, 0.86, 0.87) and chromosome 22q loss (0.74, 0.84, 0.86). Similar patterns were also observed for the other tumors (Fig. 2e). This observation demonstrates that although some meningiomas have the potential to exhibit considerable neoplastic transcriptional heterogeneity over space, chromosome 22q and 1p losses appear to remain comparatively stable. Follow-up confirmation with large, multi-institutional cohorts will be needed to confirm this finding.

Bulk methylation validates the regional consistency in meningioma biomarkers

The regional stability of meningioma biomarkers was validated with bulk DNA methylation on 19 samples from the 'internal regional' cohort tumors (including all 12 with snRNA-seq). Chromosome 1p and 22q arm-level copy number values were highly stable within the same tumor, as were methylation-inferred outcome risk scores[28,29] (Fig. 2f and Supplementary Note). Other chromosome arm gains or losses were also similar between snRNA-seq and methylation (Extended Data Fig. 4) and generally consistent within a particular meningioma (Extended Data Fig. 5 and Supplementary Note). This reinforces the observation that genomic biomarkers remain largely stable across meningiomas despite the observed neoplastic heterogeneity in some cases, supporting the notion that a single tissue sample is probably sufficient for clinical purposes. Nevertheless, it is noteworthy that within our atlas cohort, three cases that were discordant between snRNA-seq and methylation-defined chromosome 22/1p losses appeared to have possible evidence of internal heterogeneity in chromosome 1p ($n = 2$) or chromosome 22q ($n = 1$) status within the same tumor (Fig. 2g and Supplementary Note), suggesting a need for larger regionally sampled cohorts to more definitively explore the potential for rare copy number heterogeneity in meningioma.

Chromosome 22q and 1p loss incurs greater spatial neoplastic heterogeneity

Given that some meningiomas exhibited considerable regionally driven neoplastic transcriptional heterogeneity despite comparatively stable copy number alterations, we next leveraged spatial transcriptomics to further explore this spatial heterogeneity locally. For each sample ($n = 43$), Moran's index (a measure of spatial autocorrelation) was used to represent the spatial heterogeneity of each neoplastic MP. The MP5 (TNF-like) MP was associated with the highest median Moran's index overall (0.27; range, 0.07–0.58), suggesting that it is an important correlate of regional neoplastic heterogeneity. This was also the MP with the highest neoplastic *F*-statistic in P3 (internal regional cohort). Interestingly, we found that tumors with methylation-defined chromosome 1p and 22q losses were associated with higher Moran's indices in multiple neoplastic MPs. Specifically, the presence of chromosome 22q loss was associated with higher Moran's index for MP1 (cycling), MP3 (IFN-like), MP4, MP6 (EMT1), MP7 (inflammatory), MP8 and MP9 (EMT2; $P < 0.05$ for all cases, comparing 22q loss vs 22q neutral). Similarly, the presence of chromosome 1p loss was associated with higher Moran's index for MP1 (cycling), MP3 (IFN-like), MP7 (inflammatory), MP9 (EMT2), MP10 (EMT3) and MP11 (metabolic; $P < 0.05$; Fig. 2h). This finding suggests that the presence of these alterations is correlated with increased regional neoplastic transcriptional heterogeneity, which may, in part, help explain the comparatively poor outcomes and treatment resistance exhibited by tumors with these alterations.

Spatially informed sampling provides insight into the immune reprogramming of meningioma

We next sought to understand how meningioma cell states may vary between the tumor itself and its surrounding non-tumor-associated tissue. Although roughly 10% of meningiomas invade underlying brain tissue[30,31], almost all are physically connected to dura[32]. We therefore sought to study this dural attachment to gain insights into a possible source of tumor recurrence after surgery. To do so, we procured a 'spatial dura' snRNA-seq cohort, comprising one tumor sample and multiple surrounding dural samples per patient (Fig. 3a). In total, 156,480 cells from 33 samples were generated, partially overlapping with the atlas cohort (Fig. 3b). We also compared our results to normal-appearing dura samples collected from two patients with GBM, in which no dural attachment was present ($n = 6{,}893$ additional cells). Neoplastic cells were most common in the tumor and overlying dura, representing 44.5% and 53.5% of cells, respectively, decreasing to 6.0% of cells in the peripheral or marginal dura and <1% in both the 1 cm and 2 cm dural margins (chi-squared $P < 2.2 \times 10^{-22}$). By comparison, fibroblasts and endothelial cells were more common in the normal-appearing dura, representing 76.2% and 19.8% of cells in the 2 cm dura, respectively. Importantly, myeloid cells accounted for <5% of cells from the adjacent and overlying dura samples (4.5% in overlying dura, 3.4% in peripheral dura, 3.3% in 1 cm dura and 2.7% in 2 cm dura; Fig. 3c) but accounted for 42.7% of cells in the tumor samples. This expansion of the myeloid cell population in tumors suggests a potential role of myeloid cell recruitment in the pathogenesis or maintenance of meningioma.

We next sought to explore whether this marked difference in myeloid cell abundance between dura and tumor was associated with differences in transcriptional MPs. We first performed unsupervised clustering of all myeloid cells in the 'spatial dura' cohort after patient-wise batch correction to remove inter-individual variations. Strikingly, we identified a clear separation between myeloid cells obtained from tumor and those sampled from overlying or adjacent dura (Fig. 3d). Two dominant gene programs were identified:

Fig. 3 | Spatially resolved snRNA-seq and spatial transcriptomics reveals increased myeloid abundance and shifts in myeloid MP expression from dura to tumor. a, Graphical depiction of the sampling approach taken in our 'spatial dura' cohort. Created in BioRender; Singh, O. https://BioRender.com/ktepotx (2026). **b**, UMAP representation of this cohort, with each cell annotated based on type (left) and region of collection (right). GBM dura, normal-appearing dura collected from two patients with glioblastoma. **c**, Relative proportion of cell types by location of sample collection (T, tumor; OD, overlying dura; PD, peripheral dura; 1, 1 cm dura; 2, 2 cm dura). **d**, Patient-wise batch-corrected UMAP of all myeloid cells in our spatial dura cohort, with cells annotated by sample location. Individual location-specific UMAPs are plotted for clarity (right). **e**, Expression of a TNF-like program and a metabolic-like program, identified based on clustering of genes with Moran's $q < 0.001$. Note the former is predominantly expressed among the non-tumor-derived cells, whereas the reverse is true of the latter (inset boxplots; $n = 3{,}780$ dura cells; 21,219 tumor cells; two-sided t-test $P < 2.2 \times 10^{-16}$ for both plots). **f**, Relative presence of myeloid cell states by sample location. G, glioblastoma control. **g**, Relative expression of myeloid MPs by sample location (pseudobulk; $n = 7$ T, 7 OD, 4 PD, 7 1 cm, 6 2 cm, 2 G). **h**, Patient-wise batch-corrected UMAP of all neoplastic cells in our spatial dura cohort, with cells annotated by sample location. **i**, Stacked barplots for each sample with at least 50 neoplastic cells in at least one dura sample, depicting the relative proportion of cells with each permutation of chromosome 22q and 1p neutral or loss. **j**, Representative H&E slide of a sample with a preserved meningioma-tumor border, profiled with Visium HD (top). Annotation of each myeloid cell by its distance to the segmented dural border on the same sample (bottom). This same analysis was performed on three total slides with an intact tumor–dura border. **k**, Scatterplots comparing the expression of the TNF myeloid MP as a function of median binned distance from the dural border, for each of the three samples with a preserved tumor–dura border. Fitted linear regression lines and Pearson correlation values for the first 2 mm are presented, with the shaded area corresponding to the 95% confidence interval of the regression line; two-sided *P* values are shown. The median expression across all myeloid cells in cases without a dural border present is indicated by the large green dot. For all boxplots, center lines represent the median and the box spans the interquartile range (25th–75th percentile); whiskers extend to the most extreme values within 1.5 times the interquartile range beyond the quartiles.

https://doi.org/10.1038/s41588-026-02615-w

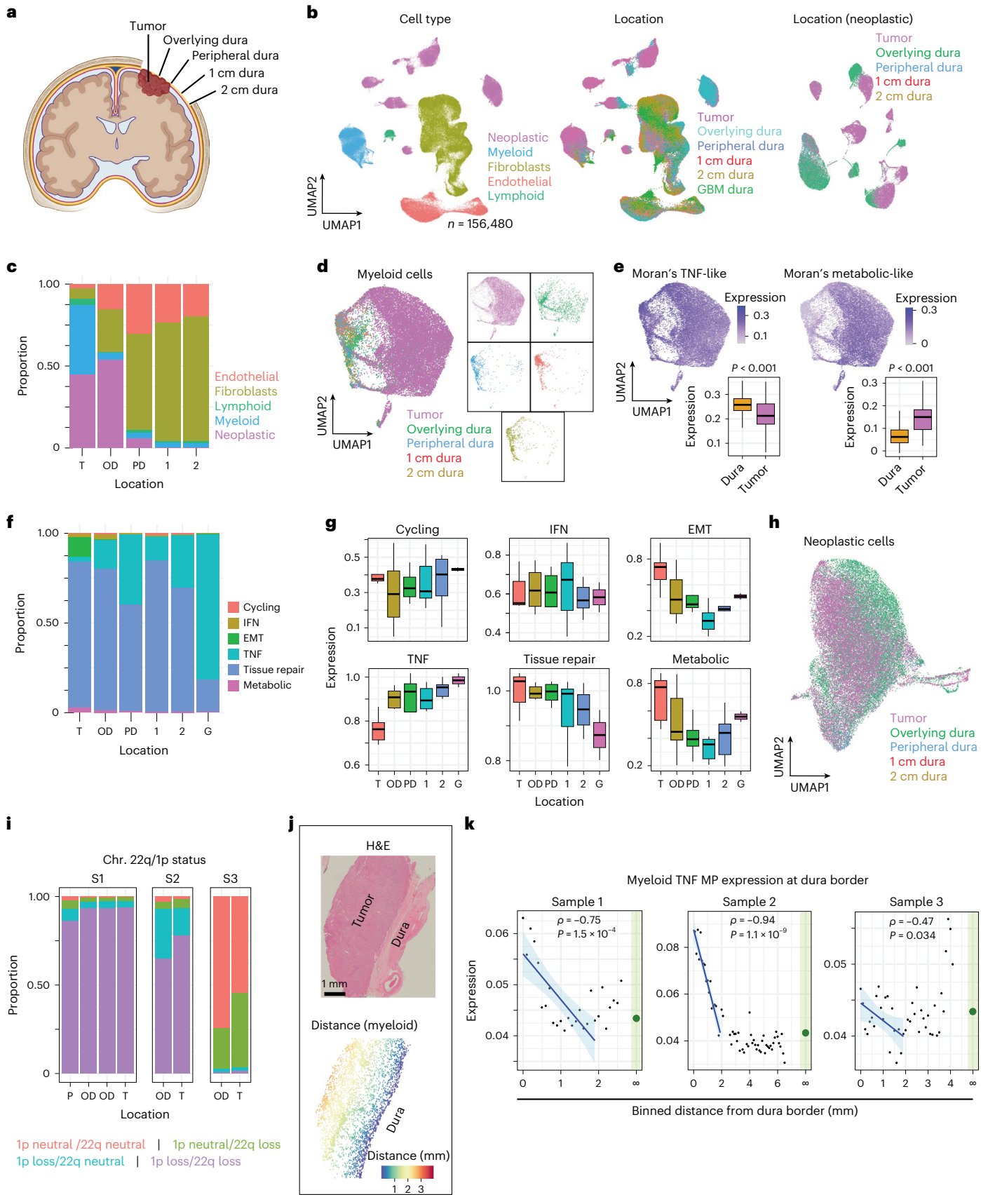

one associated with TNF pathway-related genes (upregulated in dura-derived myeloid cells) and the other associated with genes related to metabolism (upregulated in the tumor-derived myeloid cells; Fig. 3e). Within our established myeloid cell states, we also found that TNF myeloid cells were most common in dura samples from patients with GBM, representing 80.7% of myeloid cells in these samples compared to only 2.6% of myeloid cells from meningioma tumors and 12.3–39.2% of myeloid cells from underlying or adjacent dura samples. Contrarily, metabolic myeloid cells were most common within tumors, representing 2.6% of myeloid cells compared to <1% in all dura samples. Similarly, the EMT state represented 11.3% of tumor-associated myeloid cells, but <1% of myeloid cells in all dura-derived samples (Fig. 3f). Pseudobulk analysis, allowing for sample-level comparisons, yielded similar findings, with the EMT and metabolic MP significantly upregulated in tumor compared to dura samples ($P < 0.001$ and $P = 0.005$, respectively), while the TNF MP was strongly suppressed in tumor ($P = 0.002$) (Fig. 3g). Interestingly, this clear difference in MP expression between tumor and dura-derived myeloid cells was not observed in other cell types, suggesting a particular role for myeloid reprogramming in meningioma pathogenesis (Fig. 3h, Supplementary Fig. 12a and Supplementary Note).

The myeloid TNF MP is suppressed across the dura–tumor interface

Given the observed differences in myeloid states between meningioma and dura by snRNA-seq, we next leveraged our spatial transcriptomics cohort to explore the transcriptional evolution of myeloid MPs across the meningioma–dura border itself, which was present in three Visium HD samples (Supplementary Fig. 12b). Computing average myeloid MP expression at each 100 µm bin from the dural border (Fig. 3j), we found that the TNF MP was consistently negatively correlated with distance over the first 2 mm from the dural border (Fig. 3k and Supplementary Note). This indicates that the TNF MP is suppressed over very short physical distances within the meningioma tumor compared to its surrounding dura, suggesting the importance of downregulating this myeloid MP for meningioma development and progression.

Myeloid–neoplastic interactions are state-specific and influence the tumor microenvironment

Given the observation that myeloid cells found in meningioma tumors are distinct from those found in the surrounding dura and that they also differ according to tumor biology and aggressiveness (MG and WHO grade), we reasoned that myeloid cells have a role in meningioma progression through state-specific myeloid–neoplastic interactions, as has been shown in other brain tumors[16–18]. Indeed, we used CellChat[33] to infer multiple myeloid (ligand)–neoplastic (receptor) interactions that were specific to each myeloid state, including multiple that have previously been associated with cancer progression and/or the establishment of a pro-tumoral microenvironment, suggesting a potential targetable role for myeloid cells in meningioma progression[34–45] (Fig. 4a,b and Supplementary Note).

The cell state-specificity of myeloid–neoplastic interactions was further explored with spatial transcriptomics to assess whether myeloid states may induce unique transcriptional changes in surrounding neoplastic cells, or vice versa (Fig. 4c). For each myeloid cell in our cohort ($n = 603{,}414$), the expression of its MPs was correlated to the average value of all genes from all neoplastic cells within a neighborhood of radius 50 µm (Fig. 4d and Supplementary Note). Neoplastic genes that correlated with a particular local myeloid MP were termed 'MP-correlated genes'. Interestingly, we found that cycling, IFN/surveillance and metabolic MP-correlated genes were largely unique, whereas considerable overlap was identified between the EMT, TNF and tissue repair MP-correlated genes; there were also some shared genes with the metabolic program (Fig. 4e and Supplementary Note). This uniqueness of neoplastic gene expression profiles as a function of their nearby myeloid cell states reinforces the presence of state-specific myeloid–neoplastic interactions.

To further explore the function of these neoplastic MP-correlated genes, we compared them to the genes that define each myeloid MP. Surprisingly, we found that many neoplastic genes that correlated to the IFN and TNF myeloid MPs were the same as those that actually defined the myeloid IFN and TNF MPs (0.68 and 0.57 overlap indices, respectively), with lesser overlap also identified in analogous comparisons for the cycling MP (0.17), the tissue repair MP (0.16) and the metabolic MP (0.21) (Fig. 4f). This observation suggests that myeloid cells not only influence nearby neoplastic cells to exhibit unique expression profiles, but that these expression profiles resemble the expression profile of the myeloid cells themselves. Similar patterns were observed when repeating this analysis with 25 µm and 100 µm neighborhood sizes (Supplementary Fig. 13a).

Finally, we used the deep-learning-based spatial transcriptomics tool CellNEST[46] to identify recurrent and spatially informed receptor–ligand interactions between myeloid and neoplastic populations. Notably, the most state-specific interactions strongly aligned with the expected biology of each cell state (Fig. 4g and Supplementary

Fig. 4 | Each myeloid cell state is associated with unique neoplastic–myeloid interactions and spatial dependencies. a, Myeloid state-specific receptor–ligand interactions with neoplastic cells overall. The left tileplot depicts interactions in which myeloid cells express ligands and neoplastic cells express receptors, and the right tileplot depicts interactions in which neoplastic cells express ligands and myeloid cells express receptors. Only interactions with $P < 0.01$ (one-sided permutation test as implemented in CellChat) are shown. Interaction strength is proportional to tile color. **b**, Myeloid state-specific expression of various ligands and receptors identified using CellChat ($n = 685$ cells MP1; 2,062 MP2; 5,890 MP3; 5,509 MP4; 50,374 MP5; 22,962 MP6). **c**, Graphic depicting cell type assignments within a single Visium HD slide (inset H&E image; single example from 43 similar samples). **d**, Graphic illustration demonstrating the principle of myeloid neighborhood analysis, whereby the expression of all neoplastic cells within 50 µm of a particular myeloid cell is averaged (repeated on all 43 Visium HD samples). **e**, Symmetric heatmap depicting the degree of overlap (overlap coefficient) between myeloid MP-correlated neoplastic genes. **f**, Heatmap depicting the overlap coefficient between myeloid MP-correlated neoplastic genes and myeloid MP-defining genes. **g**, Heatmaps depicting the top three myeloid state-specific receptor–ligand interactions between myeloid and neoplastic cells based on the greatest associated change in myeloid MP expression compared to baseline of all interactions present in at least 50 myeloid–neoplastic pairs. Only values with adjusted $P < 0.05$ (two-sided Wilcoxon-rank sum test adjusted using the Benjamini–Hochberg method). Two interactions from the left heatmap (myeloid ligands to neoplastic receptors) are also present in the snRNA-seq (CellChat) data and are highlighted in red. **h**, CellChat output interactions ($P < 0.01$ by one-sided permutation test) that overlap with significant outputs from the CellNEST output (neoplastic ligands and myeloid receptors). Example cases of myeloid MP expression stratified by the presence of these interactions are plotted to the right ($n = 58$ cells with PROS1_MERTK vs 185,228 without; 71 with GAS6_MERK vs 185,215 without; 378 with APP_TNFRSF21 vs 184,908 without). Asterisks (*) indicate interactions that are also upregulated in the CellNEST analysis (adjusted $P < 0.05$, analogous to the values presented in **g**). **i**, Heatmap depicting the Pearson correlation coefficient between myeloid MP expression and local myeloid and neoplastic cell density (top), calculated using a 2D density kernel estimation. Analogous correlation matrix of neoplastic MPs (bottom). **j**, Boxplot depicting average CRAWDAD z-scores (generated by binomial proportion testing comparing observed neighborhoods to shuffled null backgrounds) across all samples with myeloid cells as reference and neoplastic cells as targets ($n = 43$ samples per distance). Horizontal red lines are plotted at $z = \pm 1.96$, indicating statistical significance. **k**, Output of the Ripley's inhomogeneous L-function from myeloid to neoplastic cells relative to distance (r). The line represents the mean value at all distances; the shaded area represents one standard deviation. For all boxplots in this figure, center lines represent the median and the box spans the interquartile range (25^{th}–75^{th} percentile); whiskers extend to the most extreme values within 1.5 times the interquartile range beyond the quartiles.

https://doi.org/10.1038/s41588-026-02615-w

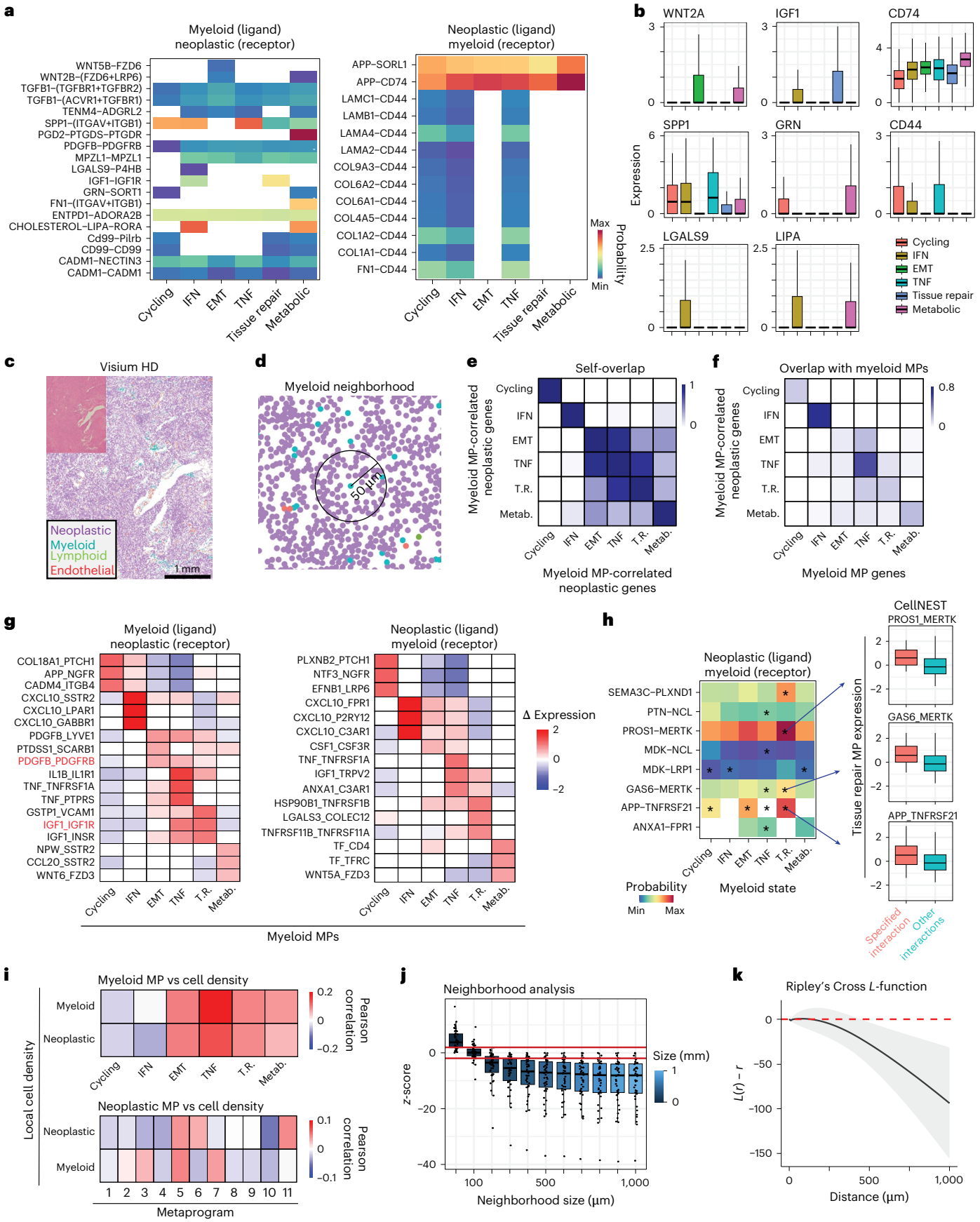

https://doi.org/10.1038/s41588-026-02615-w

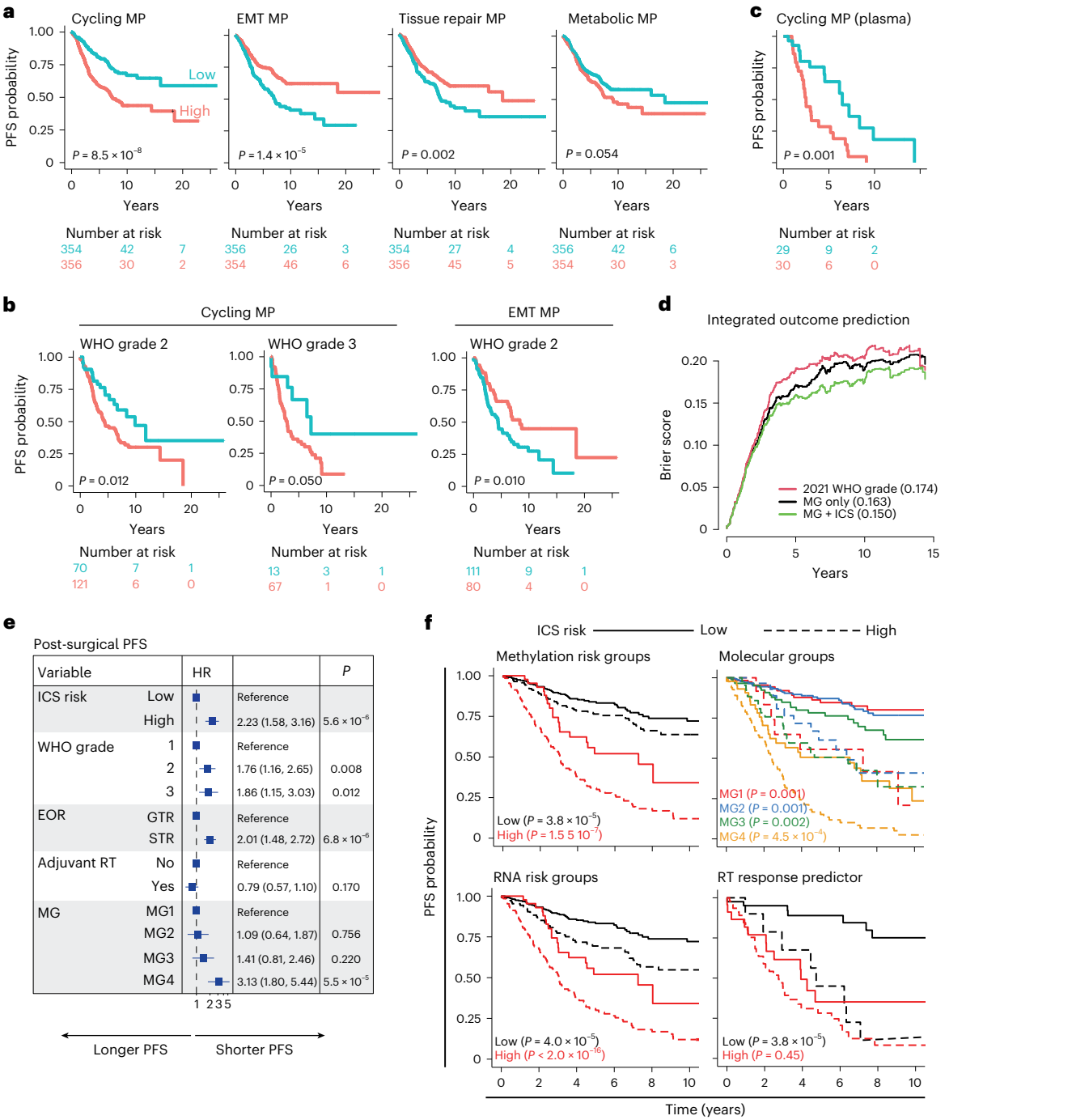

Fig. 5 | Multiple cell states are prognostic and can be used to refine outcome prediction beyond existing molecular tools. a, Kaplan–Meier curves depicting progression-free survival outcomes of patients when stratified by the median expression of multiple myeloid MPs. **b**, Kaplan–Meier curves depicting progression-free survival outcomes of a subset of patients from **a**, stratified by WHO grade. **c**, Kaplan–Meier curve depicting outcomes stratified by the median plasma methylation signature of the cycling myeloid MP. **d**, Brier curves comparing outcome prediction error based on WHO grade alone, MG alone and the integration of MG and seven prognostic MPs. **e**, Forrest plot depicting outputs of a multivariable Cox regression model with post-surgical PFS as the target variable and ICS risk group, WHO grade, extent of resection (EOR), receipt of adjuvant radiotherapy (RT) and MG as regressors. *P* values were generated from the Wald test (two-sided). **f**, Kaplan–Meier curves depicting the added outcome granularity provided by the ICS risk groups in the context of existing bulk molecular classification tools. Each subgroup is further stratified by ICS risk, with dotted lines representing high risk and solid lines representing low risk. Notably, the Kaplan–Meier on the bottom right includes only cases that underwent adjuvant RT, with outcome representing time to recurrent post RT ($n = 122$). Two-sided log-rank *P* values are presented in **a**, **b**, **c** and **f**.

Note). Comparing inferred receptor–ligand interactions from CellNEST to those inferred from snRNA-seq, the IGF1 (myeloid)–IGF1R (neoplastic) interaction was strongly associated with the tissue repair MP in both data types, reinforcing its relevance to this myeloid state (Fig. 4a,g). Multiple interactions involving myeloid receptors were also present in both data types, most commonly involving the tissue repair MP, including two involving the MERTK receptor (Fig. 4h and Supplementary Note).

https://doi.org/10.1038/s41588-026-02615-w

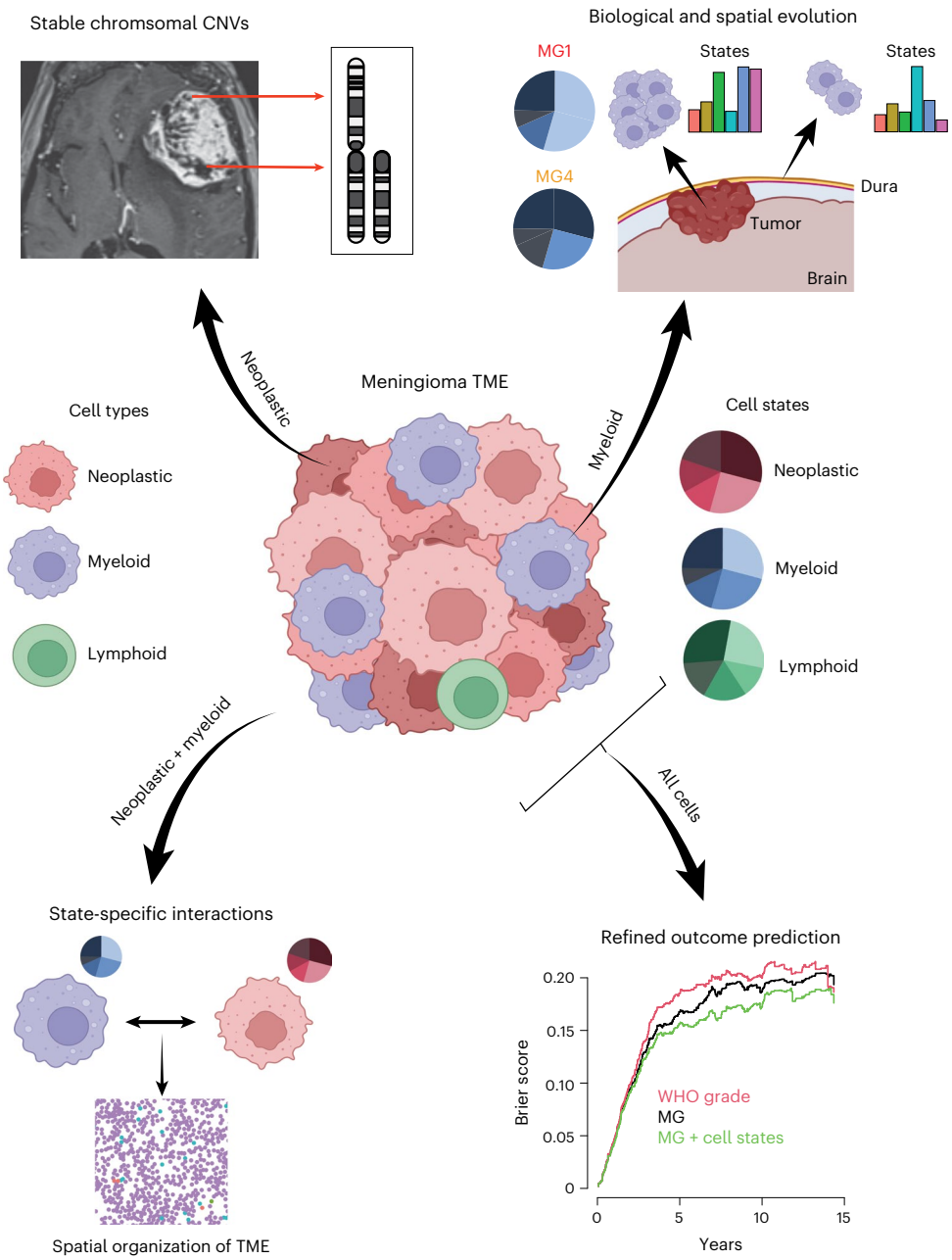

Fig. 6 | Graphical overview of findings. Profiling of the meningioma tumor microenvironment at high resolution yielded insights into the spatial variability of clinically important chromosomal alterations, the evolution of myeloid cell states between molecular groups and across the meningioma–dura border, the complexity and spatial dependence of interactions between neoplastic and myeloid cells, and the influence of cell states on clinical behavior and patient outcomes. CNV, copy number variation; MG, molecular group; TME, tumor microenvironment; WHO, World Health Organization. Created in Biorender; Singh, O. https://BioRender.com/ndzpiwq (2026).

Interestingly, we also found that myeloid and neoplastic MP expression correlated with both myeloid and neoplastic cell density (Fig. 4i). Specifically, local density of both cell types correlated most strongly with the myeloid TNF MP, with weak positive associations also noted with the EMT, tissue repair and metabolic MPs. Taken together, these findings demonstrate that myeloid cells have an important role in shaping the meningioma microenvironment, which may explain the observed tumor-specific differences in myeloid recruitment and activation.

Spatial transcriptomics reveals global spatial dependencies between cell types

We next explored global spatial dependencies within the meningioma microenvironment (see Supplementary Note for details). We found that neoplastic cells clustered around myeloid cells at small scales but dispersed over large scales (Fig. 4j,k). Analysis of lymphoid and endothelial cells further suggested the presence of 'immune-active' regions involving all non-neoplastic cells as well as 'neoplastic-rich' areas with comparatively few non-neoplastic cells (Supplementary Fig. 13b). Notably, the cell density analysis (Fig. 4i) identified two neoplastic MPs correlated with neoplastic, but not myeloid, cell density (MP6 (EMT1) and MP11 (metabolic)), suggesting that they are preferentially enriched in the neoplastic-rich regions. This finding provides insight into global patterns of meningioma organization, suggesting that the influence of myeloid cells on neoplastic cells may be largely relegated to so-called 'immune-active' regions.

Meningioma cell states are prognostic, independent of MG and cell abundance

Having demonstrated differences in myeloid states between meningioma MGs and WHO grade, as well as state-dependent myeloid–neoplastic interactions, we sought to directly explore the role of myeloid cells on meningioma progression. Myeloid-specific expression was deconvolved from our bulk RNA cohort and per-sample MPs quantified using ssGSEA. The cycling and metabolic MPs were both associated with shorter progression-free survival (PFS) in a multivariable Cox regression analysis after adjusting for MG (hazard ratio (HR), 4.04 (1.27–12.86), $P = 0.018$ and 194.84 (10.90–3,485.34), $P = 3.4 \times 10^{-4}$, respectively). By contrast, the EMT and tissue repair MPs were protective in analogous models (HR, 0 (0–0.13), $P = 0.005$ and 0.12 (0.01–1.0), $P = 0.05$; Supplementary Fig. 14a and Fig. 5a). Dichotomizing all cases by median MP expression, the cycling MP identified high-risk and low-risk cases within both WHO grade 2 and 3 cases that were associated significantly different median PFS (4.38 (95% CI, 3.22–6.80) vs 9.87 (6.11–infinity) years, $P = 0.012$ and 2.9 (2.05–4.84) vs 7.2 (3.81–infinity) years, $P = 0.050$, respectively). The EMT MP also significantly stratified WHO grade 2 cases (median PFS 4.43 (3.08–6.56) vs 8.35 (6.66–infinity) years, $P = 0.010$; Fig. 5b). The neoplastic and lymphoid metabolic MPs were also independently associated with shorter PFS, as was the lymphoid cycling MP (Supplementary Fig. 14b,c). Importantly, each of these MPs remained significantly prognostic when adjusting for the inferred proportion of their respective cell type ($P < 0.05$ for all cases), whereas none of the cell type abundances themselves were prognostic after adjusting for MG. Moreover, using a small cohort of 59 patients, we demonstrated as a proof of principle that robust signatures for each prognostic myeloid MP could be generated from plasma methylation (Extended Data Fig. 6) and that the plasma-inferred cycling myeloid MP remained prognostic (Fig. 5c), suggesting potential utility for such non-invasive biomarkers (details in Supplementary Note). We conclude that the meningioma microenvironment is a diverse ecosystem with major influence from myeloid cells, whose activation states are deeply associated with meningioma behavior at a clinical level.

Integrating meningioma cell states can refine outcome predictions in addition to existing MGs

We next sought to integrate individually prognostic MPs to refine the existing outcome prediction afforded by WHO grade or MG. An elastic net regularized Cox model identified seven MPs (myeloid EMT, TNF, tissue repair and metabolic; neoplastic inflammatory; and lymphoid cycling and metabolic) and MG as prognostic features. Adding these variables to Cox regression models resulted in improved Brier error compared to analogous models based on MG or WHO grade alone (Fig. 5d). Finally, we developed an integrated cell state (ICS) score by computing a weighted sum of the above seven MPs with their respective Cox model coefficients, which was then dichotomized into ICS risk groups (high vs low). These groups were strongly prognostic after adjusting for WHO grade, extent of resection, receipt of adjuvant radiotherapy and MG (HR, 2.23 (95% CI, 1.58–3.16), $P = 5.6 \times 10^{-6}$; Fig. 5e). They also added considerable granularity to outcome predictions afforded by existing molecular outcome prediction models (methylation risk groups, MGs and RNA-defined risk groups) generated using bulk data (log-rank $P < 0.05$ for ICS-high vs ICS-low within each subgroup; Fig. 5f). Examining only the subset of cases that received adjuvant radiotherapy ($n = 122$), we found that the ICS risk groups identified a subset of predicted radiotherapy-sensitive cases (based on our previously published model[8]) that were associated with poor outcomes (log-rank $P < 0.001$ ICS-low vs ICS-high), suggesting a role in radiotherapy response prediction (Fig. 5f). Overall, this observation suggests that the cell state composition of the meningioma microenvironment, inferable with bulk RNA-seq, imparts strong influence on tumor progression, allowing for increasingly refined outcome prediction in addition to what is achieved by modern MGs of meningioma alone.

Discussion

We present a large single-cell-resolution genomics atlas of meningioma, with more than 500,000 high-quality nuclei strategically collected to represent the full breadth of MGs and spatial regions within and surrounding a meningioma. Our spatial transcriptomics cohort generated data for an additional seven million individually segmented cells to allow insights into the regional variability within the meningioma microenvironment, and an additional 712 cases with bulk DNA methylation and RNA-seq allowed for additional validation and correlation to clinical outcomes. Integration of proteomics ($n = 88$) and plasma methylation ($n = 59$) data allowed for further validation and translational value.

By deeply characterizing all meningioma cell types, we have identified an appreciation for the heterogeneity and clinical importance of multiple cell types and states, with a focus on the myeloid population, which exhibits marked transcriptional heterogeneity, regional evolution, state-dependent interactions with the local microenvironment and prognostic influence (Fig. 6 and Supplementary Note). Our work also demonstrates the profound complexity of the meningioma microenvironment, highlighting the urgent need for faithful tumor-microenvironment-preserving preclinical models to translate these findings into actionable therapeutics.

Online content

Any methods, additional references, Nature Portfolio reporting summaries, source data, extended data, supplementary information, acknowledgements, peer review information; details of author contributions and competing interests; and statements of data and code availability are available at https://doi.org/10.1038/s41588-026-02615-w.

References

1. Ostrom, Q. T. et al. CBTRUS statistical report: primary brain and other central nervous system tumors diagnosed in the United States in 2015–2019. *Neuro. Oncol.* **24**, v1–v95 (2022).
2. Wang, J. Z. et al. Meningioma: International Consortium on Meningiomas (ICOM) consensus review on scientific advances & treatment paradigms for clinicians, researchers, and patients. *Neuro. Oncol.* https://doi.org/10.1093/neuonc/noae082 (2024).
3. Wang, J. Z. et al. The multiomic landscape of meningiomas: a review and update. *J. Neurooncol.* **161**, 405–414 (2023).
4. Nassiri, F. et al. A clinically applicable integrative molecular classification of meningiomas. *Nature* **597**, 119–125 (2021).
5. Driver, J. et al. A molecularly integrated grade for meningioma. *Neuro. Oncol.* **24**, 796–808 (2022).
6. Landry, A. P. et al. Development and validation of a molecular classifier of meningiomas. *Neuro. Oncol.* https://doi.org/10.1093/neuonc/noae242 (2025).
7. Landry, A. P. et al. Chromosome 1p loss and 1q gain for grading of meningioma. *JAMA Oncol.* https://doi.org/10.1001/jamaoncol.2025.0329 (2025).
8. Wang, J. Z. et al. Molecular classification to refine surgical and radiotherapeutic decision-making in meningioma. *Nat. Med.* https://doi.org/10.1038/s41591-024-03167-4 (2024).
9. Sahm, F. et al. cIMPACT-NOW update 8: clarifications on molecular risk parameters and recommendations for WHO grading of meningiomas. *Neuro. Oncol.* https://doi.org/10.1093/neuonc/noae170 (2024).
10. Maas, S. L. N. et al. Integrated molecular-morphologic meningioma classification: a multicenter retrospective analysis, retrospectively and prospectively validated. *J. Clin. Oncol.* **39**, 3839–3852 (2021).
11. Lucas, C.-H. G. et al. Spatial genomic, biochemical and cellular mechanisms underlying meningioma heterogeneity and evolution. *Nat. Genet.* **56**, 1121–1133 (2024).

12. Choudhury, A. et al. Meningioma DNA methylation groups identify biological drivers and therapeutic vulnerabilities. *Nat. Genet.* **54**, 649–659 (2022).
13. Bayley, J. C. et al. Multiple approaches converge on three biological subtypes of meningioma and extract new insights from published studies. *Sci. Adv.* **8**, eabm6247 (2022).
14. Sahm, F. et al. DNA methylation-based classification and grading system for meningioma: a multicentre, retrospective analysis. *Lancet Oncol.* **18**, 682–694 (2017).
15. Choudhury, A., Chen, W., Lucas, C.-H., Magill, S. & Raleigh, D. Path-35. Hypermitotic meningiomas harbor DNA methylation subgroups with distinct biological and clinical features. *Neuro. Oncol.* **24**, vii158–vii158 (2022).
16. Miller, T. E. et al. Programs, origins and immunomodulatory functions of myeloid cells in glioma. *Nature* **640**, 1072–1082 (2025).
17. Maas, R. R. et al. The local microenvironment drives activation of neutrophils in human brain tumors. *Cell* **186**, 4546–4566.e27 (2023).
18. Klemm, F. et al. Interrogation of the microenvironmental landscape in brain tumors reveals disease-specific alterations of immune cells. *Cell* **181**, 1643–1660.e17 (2020).
19. de Visser, K. E. & Joyce, J. A. The evolving tumor microenvironment: from cancer initiation to metastatic outgrowth. *Cancer Cell* **41**, 374–403 (2023).
20. Shen, S. Y. et al. Sensitive tumour detection and classification using plasma cell-free DNA methylomes. *Nature* **563**, 579–583 (2018).
21. Nassiri, F. et al. Detection and discrimination of intracranial tumors using plasma cell-free DNA methylomes. *Nat. Med.* **26**, 1044–1047 (2020).
22. Shen, S. Y., Burgener, J. M., Bratman, S. V. & De Carvalho, D. D. Preparation of cfMeDIP-seq libraries for methylome profiling of plasma cell-free DNA. *Nat. Protoc.* **14**, 2749–2780 (2019).
23. Ke, C. et al. Secreted clusterin inhibits tumorigenesis by modulating tumor cells and macrophages in human meningioma. *Neuro. Oncol.* **26**, 1262–1279 (2024).
24. Lee, J. Y. et al. Single-cell analysis reveals a longitudinal trajectory of meningioma evolution and heterogeneity. *Nat. Commun.* **16**, 5481 (2025).
25. Wang, A. Z. et al. Single-cell profiling of human dura and meningioma reveals cellular meningeal landscape and insights into meningioma immune response. *Genome Med.* **14**, 49 (2022).
26. Zhang, J. et al. Re-analysis of single-cell RNA-seq data reveals the origin and roles of cycling myeloid cells. *Stem Cells* **42**, 593–606 (2024).
27. Lee, C.-F. et al. Preventing allograft rejection by targeting immune metabolism. *Cell Rep.* **13**, 760–770 (2015).
28. Landry, A. P. et al. Validation and next-generation update of a DNA methylation-based recurrence predictor for meningioma: a multicenter prospective study. *Neuro. Oncol.* https://doi.org/10.1093/neuonc/noae236 (2024).
29. Nassiri, F. et al. DNA methylation profiling to predict recurrence risk in meningioma: development and validation of a nomogram to optimize clinical management. *Neuro. Oncol.* **21**, 901–910 (2019).
30. Spille, D. C. et al. Brain invasion in meningiomas: incidence and correlations with clinical variables and prognosis. *World Neurosurg.* **93**, 346–354 (2016).
31. Rebchuk, A. D. et al. The impact of brain invasion criteria on the incidence and distribution of WHO grade 1, 2, and 3 meningiomas. *Neuro. Oncol.* **24**, 1524–1532 (2022).
32. Zhang, J., Chi, L., Meng, B., Li, F. & Zhu, S. Meningioma without dural attachment: case report, classification, and review of the literature. *Surg. Neurol.* **67**, 535–539 (2007).
33. Jin, S. et al. Inference and analysis of cell–cell communication using CellChat. *Nat. Commun.* **12**, 1088 (2021).
34. Rhost, S. et al. Sortilin inhibition limits secretion-induced progranulin-dependent breast cancer progression and cancer stem cell expansion. *Breast Cancer Res.* **20**, 137 (2018).
35. Wang, C. et al. SPP1 represents a therapeutic target that promotes the progression of oesophageal squamous cell carcinoma by driving M2 macrophage infiltration. *Br. J. Cancer* **130**, 1770–1782 (2024).
36. Tigue, M. L. et al. Wnt signaling in the phenotype and function of tumor-associated macrophages. *Cancer Res.* **83**, 3–11 (2023).
37. Sumitomo, R. et al. Wnt2b and Wnt5a expression is highly associated with M2 TAMs in non-small cell lung cancer. *Oncol. Rep.* **48**, 189 (2022).
38. Avşar, G. & Pir, P. An integrated study to decipher immunosuppressive cellular communication in the PDAC environment. *NPJ Syst. Biol. Appl.* **9**, 56 (2023).
39. Alfaro-Arnedo, E. et al. IGF1R acts as a cancer-promoting factor in the tumor microenvironment facilitating lung metastasis implantation and progression. *Oncogene* **41**, 3625–3639 (2022).
40. Spadaro, O. et al. IGF1 shapes macrophage activation in response to immunometabolic challenge. *Cell Rep.* **19**, 225–234 (2017).
41. Gerloff, D. et al. Melanoma-derived exosomal miR-125b-5p educates tumor associated macrophages (TAMs) by targeting lysosomal acid lipase A (LIPA). *Cancers (Basel)* **12**, 464 (2020).
42. Zhang, X. et al. Tumor-associated M2 macrophages in the immune microenvironment influence the progression of renal clear cell carcinoma by regulating M2 macrophage-associated genes. *Front. Oncol.* **13**, 1157861 (2023).
43. Ma, C. et al. Therapeutic modulation of APP–CD74 axis can activate phagocytosis of TAMs in GBM. *Biochim. Biophys. Acta Mol. Basis Dis.* **1870**, 167449 (2024).
44. Ivanova, E. L. et al. CD44 expressed by myeloid cells promotes glioma invasion. *Front. Oncol.* **12**, 6989–7008 (2022).
45. Zhang, Q., Wang, X., Liu, Y., Xu, H. & Ye, C. Pan-cancer and single-cell analyses identify CD44 as an immunotherapy response predictor and regulating macrophage polarization and tumor progression in colorectal cancer. *Front. Oncol.* **14**, 1380821 (2024).
46. Zohora, F. T. et al. CellNEST reveals cell–cell relay networks using attention mechanisms on spatial transcriptomics. *Nat. Methods* **22**, 1505–1519 (2025).

Methods

Study cohort

The cohort for this study was generated using a combination of previously published cases analyzed by our group, publicly available datasets and additional cases that we obtained for this new analysis. All samples from our snRNA-seq and spatial transcriptomics cohorts were obtained from the University Health Network, Toronto. Our bulk dataset was obtained from University Health Network, Indiana University, Case Western University, the Fred Hutchinson Cancer Center, samples from the RTOG-0539 clinical trial and publicly available datasets[12,13]. This study was approved by the University Health Network Institutional Review Board (18-5820). All patients provided written and informed consent for tumor banking and analysis as well as use of de-identified clinical data for the purposes of research, as part of routine surgical consent and institutional policy.

Sample processing

Our complete cohort consisted of a combination of fresh-frozen tissue, which was immediately frozen at the time of surgery and stored at −80 °C, and formalin-fixed, paraffin-embedded tissue (FFPE). Frozen and FFPE tissues were processed for snRNA-seq (10x Genomics) and spatial transcriptomics (10x Genomics, Visium HD), respectively, at the Princess Margaret Genomics Centre. For samples in the bulk cohort that were processed locally, DNA was extracted using the DNeasy Blood and Tissue Kit or QIAamp DNA FFPE Tissue Kit (Qiagen), and RNA was extracted using the RNEasy Kit (Qiagen).

DNA methylation

For bulk DNA methylation, 250–500 ng of extracted DNA, where available, was bisulfite-converted using the EZ DNA Methylation Kit. Bisulfite-converted DNA was then profiled using the Illumina 850k EPIC array. Raw output files were preprocessed and ssNoob-normalized using the minfi[47] package (v.1.50.0). Samples with average detection *P* values of >0.05 were removed from downstream analysis. Chromosomal copy number alterations were inferred using the conumee R package (v.1.38.0), including only probes with detection *P* values of <0.01 (ref. 48). MG assignment was done using our previously published DNA methylation-based classifier[6]. Methylation risk score (probability of progression or recurrence 5 years post surgery) was also computed using our previously published model[28] and, where needed, outputs were dichotomized into high and low risk groups by maximizing Youden's index[49]. Radiotherapy response probability was also computed for samples that received adjuvant radiotherapy using our previously published model[8] and similarly dichotomized into risk groups.

RNA-seq

Paired-end sequencing was performed on extracted RNA using the Illumina HiSeq 2500 to target 70 million reads per sample. Adaptor trimming was performed using Trim Galore (v.0.5.0), and trimmed reads were aligned to the GRCh38 human reference genome using the STAR aligner (v.2.7.9a)[50]. Gene expression quantification was performed using HTSeq[51] (v.0.11.0) to generate counts for downstream analysis. Finally, the edgeR[52] package (v.4.2.1) was applied to convert these raw counts into log-transformed counts per million with trimmed mean of M normalization. Both raw counts and post-processed $\log_2$(counts per million) data were used for downstream analyses, depending on the application. We computed a gene expression risk score[53] for all samples as we have previously published[8]. Specifically, the model was trained on a publicly available UCSF cohort, using their methodologies as originally published, by computing the weighted sum of the predefined 34-gene signature with their respective LASSO-regularized Cox regression coefficient. Dichotomization into high-risk and low-risk groups was done by maximizing Youden's index.

SnRNA-seq and quality control

SnRNA-seq was performed on frozen tissue with a target of 6,000 nuclei and 60,000 reads. Nuclei were isolated using 10x Genomics Chromium Nuclei Isolation Kit lysis buffer with Miltenyi Anti-Nucleus beads and manual dissociation. Leftover tissue was removed with a nuclei isolation column, and the resultant pellet was resuspended in nuclei separation buffer. Miltenyi Anti-nucleus beads were then added to the sample, nuclei were incubated for 15 min on ice and the sample was passed through an LS column attached to the MACS MultiStand with QuadroMACS separator. Purified nuclei were washed, and a target of 10,000 nuclei was loaded onto a 10x Genomics Chromium 3′ GEM-X chip. After droplet generation, samples were transferred to a pre-chilled strip tube (USA Scientific) and incubated in a Bio-Rad thermocycler. Sample cDNA was recovered using Recovery Agent, provided by 10x Genomics, and cleaned up using a Silane DynaBead (Thermo Fisher) mix. Purified cDNA was amplified for 11 cycles before being cleaned up using SPRIselect beads (Beckman Coulter). Samples were run on a Bioanalyzer (Agilent Technologies) to determine cDNA concentration. cDNA libraries were prepared as outlined in the Chromium GEM-X Single Cell 3′ Reagent Kit v.4 user guide, with modifications to the PCR cycles based on the calculated cDNA concentration. Gene expression libraries were then sequenced on Illumina's NovaSeqX, and output was processed using the Cell Ranger pipeline (10x Genomics). In our complete cohort, the mean number of raw reads per cell was 81,154.14 with a standard deviation of 62,576.79 and a minimum of 24,111 reads. The average (s.d.) proportion of reads that mapped to the genome was 96.4% (2.6%), and the average median number of unique molecular identifiers (UMIs) per cell was 4,619.6 (2,187.7), suggesting adequate sequencing depth across our cohort.

Output raw counts were filtered to include only cells with at least 1,000 UMIs to ensure sufficient library complexity. We also excluded cells with more than 3% of transcripts belonging to mitochondrial genes to ensure that only high-quality cells were retained. Doublets were predicted and removed using scDblFinder (v.1.18.0) with default parameters[54]. Ambient RNA content was inferred using the established R packages Celda (v.1.20.0; DecontX)[55] and DIEM[56] (v.2.4.1) with default parameters, and values were compared between groups of interest.

Cell type annotation

We used multiple iterative approaches for cell type assignment. First, cell clusters with consistently large-scale copy number alterations using the InferCNV pipeline (https://github.com/broadinstitute/inferCNV; v.1.20.0) were considered neoplastic. Those that were copy-number neutral were examined using canonical cell-type-specific genes and the established gene-signature pipeline scATOMIC[57] (v.2.0.3). Copy-number-neutral clusters (based on Louvain clustering), which were specific to a particular patient and did not express myeloid, endothelial or lymphoid markers, were also assigned as neoplastic. This approach was repeated iteratively for the unlabeled cells and within each cell type to ensure robust assignments. Cells with indeterminate or inconsistent labels were removed from downstream analyses to ensure high-confidence assignments. Louvain clustering (Seurat, v.5.1.0; resolution 0.1) was also applied within cell types to validate the results of sample-wise NMF in the atlas cohort.

Cell-level copy number inference

To quantify chromosome arm-level copy number alterations for individual cells, we again used the inferCNV pipeline, with the two dura samples from patients with GBM as control tissue. For chromosome arms of interest (namely, 1p loss and 22q loss), density curves of the mean scaled arm-level deviation were generated for each sample and compared to the analogous curve generated from normal dura. This procedure was used to select an optimal, balanced cutoff with which to define a copy number loss for each chromosome arm being probed. Cells with arm-level deviation below this cutoff were then considered

to have chromosome loss, though intrinsic signal noise prohibited a threshold with perfect sensitivity and specificity.

Gene program identification with NMF

Sample-wise NMF was applied separately to each cell type in our atlas to identify intrinsic and recurrent gene programs. Only samples with at least 50 cells in a particular cell type were included to avoid bias. Rank (k) ranged from six to nine, and each individual program was defined by NMF score, using its top 50 genes. These programs were then filtered to include only those present across multiple ranks to ensure robustness and remove those that are redundant across ranks or unique to a single sample. Filtered programs were then clustered by Jaccard index to identify recurrent shared programs (clusters of programs with overlapping genes; that is, MPs). MPs were then defined based on genes present in at least 25% of their constituent programs. The expression of each MP within each cell was then computed based on these MP-specific signatures using AUCell[58] (v.1.26.0). These MPs were further validated using previously published single-cell meningioma data[23–25], and raw data were preprocessed in the same way as the study cohort. NMF was used to identify MPs within each study in the same way as they were identified in the atlas cohort. Cohorts were excluded from analysis within a particular cell type if there were fewer than four unique samples with 50 cells. Expression of each MP was then quantified in the atlas cohort using AUCell, and Pearson correlation values were generated to compare each MP to those generated from the atlas cohort.

Receptor–ligand inference

We applied CellChat[33] (v.2.1.2) to our snRNA-seq cell atlas cohort to infer putative receptor–ligand interactions curated from large established databases[59,60]. Default parameters were applied. Only high-likelihood interactions ($P < 0.01$) were included between each myeloid subtype and the neoplastic cells overall.

Bulk RNA deconvolution analysis

To estimate the relative proportion of each major cell type in the bulk RNA data and infer the cell-type-specific gene expression profiles, we used the established pipeline Bayesprism[61]. Raw counts were used as input for both bulk RNA-seq and the reference snRNA-seq data. Our atlas cohort was used to produce a cell-type-specific signature matrix for the deconvolution. Output cell-type-specific raw counts were processed as described in the 'RNA-seq' section; ssGSEA (package GSVA v.1.52.3)[62] was then used to quantify the expression of each MP from this inferred cell-type-specific RNA-seq data.

Survival analysis

To understand the prognostic role of each cell state, each cell-specific MP was quantified for each bulk RNA sample as described above. Two separate multivariable Cox regression models were constructed for each MP with progression or recurrence as the outcome of interest: one including the MP expression and MG, and one including the MP expression and the inferred abundance of its cell type across samples. This served to elucidate whether the cell state reflected known biological differences between MGs of meningioma and whether cell type abundance or cell state was more influential on outcome (that is, PFS). Kaplan–Meier curves were also generated for each independently prognostic MP with samples split by median MP expression. The log-rank test was used to determine significance.

Spatial transcriptomics

Spatial transcriptomics was performed with Visium HD according to the manufacturer's instructions. In brief, FFPE slides were deparaffinized with xylene and ethanol washes, followed by hematoxylin and eosin (H&E) staining. Glycerol was added to cover the tissue, and a coverslip was applied for imaging. The coverslip was removed immediately after imaging, and the slides were destained using HCl in a Visium cassette. After removing HCl, decrosslinking buffer was applied, followed by probe hybridization mix, which was left at 50°C for 18 h. Wash buffer was then added, followed by probe ligation mix and an additional wash buffer. Slides were then removed from the Visium cassette and stained with 10% eosin before loading onto Visium CytAssist with probe release mix. Visium HD slides were then prepared and added to the cassettes along with probe extension mix. Samples were then sequenced at five million reads per capture area using the Illumina NovaSeq. Notably, the SpaceRanger pipeline generated a mean of 432,817,149 (s.d., 81,927,495) total reads per sample with an average of 899.9 (428.7) reads and 132.8 (80.4) UMIs per 8 µm square bin, suggesting adequate sequencing depth across our samples.

The bin2cell[63] pipeline (v.0.3.3) was used to segment individual cells from high-resolution H&E images, and all overlying 2 µm spots for an individual cell were combined to yield a cell-level pseudobulk expression profile. Default parameters were used for the bin2cell pipeline, with a probability threshold set to 0.01. Each cell was annotated using Robust Cell Type Decomposition (package spacexr, v.2.2.1)[64] based on the cell-type signature matrix obtained from our atlas cohort. Only cells predicted to be singlets in this algorithm were retained, and those predicted to be either doublets or unknown were excluded from downstream analysis. For samples with a tumor-border interface present ($n = 3$), a combination of unsupervised spatially resolved clustering using the BANKSY[65] algorithm (v.1.1.0) and subsequent manual fine-tuning based on the underlying ground-truth H&E image was used to segment regions of dura. The distance from each meningioma tumor cell to the nearest dura cell was computed using the k-nearest neighbors search algorithm (get.knn)[66] in the FNN R package (v.1.1.4) and correlated with MP expression.

To explore the myeloid–neoplastic interactome in the spatial domain, we performed a neighborhood search across all myeloid cells in our cohort (excluding regions of dura or brain) using the same nn2 nearest neighbor algorithm[66] in the RANN R package (v.2.6.1). Specifically, a neighborhood was constructed around each myeloid cell, such that all neoplastic cells within 50 µm were included. For each myeloid cell, the expression of each myeloid MP was computed using AUCell, and the mean gene expression profile of all neighboring neoplastic cells was extracted. Neoplastic genes exhibiting correlation with a particular myeloid MP (Pearson correlation of >0.1) were considered MP-correlated genes. MP-correlated genes were then compared with each other and with the myeloid MP-defining genes.

Spatial transcriptomics cell–cell communication inference

To identify cell–cell communication patterns in Visium HD data, we used the graph neural network pipeline CellNEST[46] with default training parameters. To ensure that only the most robust interactions were included in downstream analysis, the top 20% of interactions for each sample were maintained as suggested in the CellNEST publication. Additionally, myeloid–neoplastic interactions were filtered if they were predicted to occur fewer than 50 times in our cohort (per direction). To ascertain interactions most specific to the expression of a particular myeloid MP, z-scaled MP expression was compared between myeloid cells involving a particular interaction and all other cells involving at least one significant interaction (to avoid bias from cells with very low expression that are not involved in any predicted interactions). Interactions associated with significantly higher expression of a particular MP (Benjamini–Hochberg-corrected P value from Wilcoxon test) were ranked by difference in mean expression to identify the interactions most strongly associated with each myeloid MP. This procedure was repeated for both directions of myeloid–neoplastic interactions (myeloid (ligand) to neoplastic (receptor) and vice versa).

Spatial co-localization analysis

The open-source R package CRAWDAD[67] (v.1.0.1) was used to quantify cell co-localization across various neighborhood sizes (50, 100, 200,

300, 400, 500, 600, 700, 800, 900 and 1,000 µm). For each sample at each length scale, a *z*-score was computed for each reference and target cell type. Three permuted null backgrounds were used for comparison to spatial randomness, and each output *z*-score was averaged. *Z*-scores outside the range (−1.96, 1.96) were considered statistically significant, with positive values associated with spatial co-localization and negative values associated with spatial depletion. Ripley's inhomogeneous *L*-cross function was also computed across the whole cohort, with myeloid cells as reference and neoplastic cells as target at 10 µm intervals of *r*, up to 1,000 µm, using the spatstat R package (v.3.3-0).

Plasma methylation profiling

Cell-free DNA (cfDNA) from each sample was extracted and processed according to our cfMeDIP-seq protocol as previously described[20,21,68], using between 2.5 and 10 ng of cfDNA per sample. Output sequencing data were trimmed and filtered using Trim Galore (v.0.5.0), cutadapt[69] (v.2.5) and fastQC (v.0.11.5). High-quality reads were aligned with the human genome using Bowtie2 (ref. 70) (v.2.3.5), deduplicated and indexed using Samtools[71] (v.1.20) and reduced to 300 bp genomic windows that map to regulatory features (CpG islands, shores, shelves and FANTOM5 enhancers) using the MEDIPS package[72] (v.1.56.0); $\log_2$-transformed counts per million were used for downstream analysis. Batch correction was done using the Combat function in the sva R package (v.3.52.0)[73].

Shotgun proteomics

For additional validation of results, we used shotgun proteomic data on a subset of cases from our bulk genomics cohort ($n = 88$), which has been described in detail and published previously[4]. Acquired data from mass spectrometry was searched using MaxQuant against a UniProt human protein sequence database with a false discovery rate of 1%. Relative label-free protein quantification was calculated with mass spectrometry peak integration, and proteins identified by at least two peptides were used for subsequent analysis. Protein expression values were $\log_2$ transformed for downstream analysis.

Differential protein abundance and pathway analysis

For each myeloid MP, all samples in the bulk genomic cohort were labeled as either high or low expression based on the median threshold, as described above. Differential protein abundance was computed between high and low cases for each MP using limma[74], and each protein was then ranked by moderated *t*-statistic, which was used as input for pathway analysis. The relative enrichment of 50 predefined hallmark gene sets (MSigDB) was computed using the FGSEA[75] package (v.1.30.0), and pathways were filtered to include those with $P < 0.05$.

Statistics and reproducibility

This is a retrospective cohort study of patients with a diagnosis of meningioma. Sample selection was based on the availability of tissue and clinical data, as well as feasibility for the collection of prospective samples with dedicated multi-regional profiling; therefore, no statistical method was used to predetermine sample size. No samples were unexpectedly excluded from our analysis.

Samples were blinded to clinical data during sample preprocessing and sequencing. The experiments were not randomized owing to the study design.

Reporting summary

Further information on research design is available in the Nature Portfolio Reporting Summary linked to this article.

Data availability

Newly generated raw sequencing data (fastq files) and associated clinical metadata have been deposited at the European Genome-Phenome Archive (https://ega-archive.org: EGAD50000002214 for cfMeDIP-seq data; EGAD50000002233 for Visium HD data; EGAD50000002272 for snRNA-seq data). Publicly available single-cell RNA-seq data were obtained from the Gene Expression Omnibus (GEO) (GSE206647 (ref. 23) and GSE278452 (ref. 24)) and Zenodo (https://doi.org/10.5281/zenodo.4932158 (ref. 25)). Proteomic data were deposited as part of a prior publication[4] to the Mass Spectrometry Interactive Virtual Environment (MassIVE; MSV000086901). Bulk DNA methylation (IDAT files) and RNA-seq (fastq files) data have been deposited from previous publications[4,8] (https://www.ncbi.nlm.nih.gov/geo: GSE180061, GSE270371; https://ega-archive.org: EGAS00001004982; https://www.ncbi.nlm.nih.gov/sra: PRJNA1127224, Database of Genotypes and Phenotypes (dbGaP): phs003707.v1.p1) or were obtained from publicly available cohorts deposited in GEO (GSE189521 (ref. 13) and GSE183656 (ref. 12)).

Code availability

All code generated as part of this work is available via Zenodo at https://doi.org/10.5281/zenodo.17874195 (ref. 76). A GitHub repository is available at https://github.com/patilvikas/Meningioma_spatial_transcriptomics.

References

47. Aryee, M. J. et al. Minfi: a flexible and comprehensive Bioconductor package for the analysis of Infinium DNA methylation microarrays. *Bioinformatics* **30**, 1363–1369 (2014).
48. Daenekas, B. et al. Conumee 2.0: enhanced copy-number variation analysis from DNA methylation arrays for humans and mice. *Bioinformatics* **40**, btae029 (2024).
49. Thiele, C. & Hirschfeld, G. cutpointr: improved estimation and validation of optimal cutpoints in R. *J. Stat. Softw.* https://doi.org/10.18637/jss.v098.i11 (2021).
50. Dobin, A. et al. STAR: ultrafast universal RNA-seq aligner. *Bioinformatics* **29**, 15–21 (2013).
51. Putri, G. H., Anders, S., Pyl, P. T., Pimanda, J. E. & Zanini, F. Analysing high-throughput sequencing data in Python with HTSeq 2.0. *Bioinformatics* **38**, 2943–2945 (2022).
52. Robinson, M. D., McCarthy, D. J. & Smyth, G. K. edgeR: a Bioconductor package for differential expression analysis of digital gene expression data. *Bioinformatics* **26**, 139–140 (2010).
53. Chen, W. C. et al. Targeted gene expression profiling predicts meningioma outcomes and radiotherapy responses. *Nat. Med.* **29**, 3067–3076 (2023).
54. Germain, P.-L., Lun, A., Garcia Meixide, C., Macnair, W. & Robinson, M. D. Doublet identification in single-cell sequencing data using scDblFinder. *F1000Res.* **10**, 979 (2022).
55. Yang, S. et al. Decontamination of ambient RNA in single-cell RNA-seq with DecontX. *Genome Biol.* **21**, 57 (2020).
56. Alvarez, M. et al. Enhancing droplet-based single-nucleus RNA-seq resolution using the semi-supervised machine learning classifier DIEM. *Sci. Rep.* **10**, 11019 (2020).
57. Nofech-Mozes, I., Soave, D., Awadalla, P. & Abelson, S. Pan-cancer classification of single cells in the tumour microenvironment. *Nat. Commun.* **14**, 1615 (2023).
58. Aibar, S. et al. SCENIC: single-cell regulatory network inference and clustering. *Nat. Methods* **14**, 1083–1086 (2017).
59. Türei, D. et al. Integrated intra- and intercellular signaling knowledge for multicellular omics analysis. *Mol. Syst. Biol.* **17**, e9923 (2021).
60. Türei, D., Korcsmáros, T. & Saez-Rodriguez, J. OmniPath: guidelines and gateway for literature-curated signaling pathway resources. *Nat. Methods* **13**, 966–967 (2016).
61. Chu, T., Wang, Z., Pe'er, D. & Danko, C. G. Cell type and gene expression deconvolution with BayesPrism enables Bayesian integrative analysis across bulk and single-cell RNA sequencing in oncology. *Nat. Cancer* **3**, 505–517 (2022).

62. Subramanian, A. et al. Gene set enrichment analysis: a knowledge-based approach for interpreting genome-wide expression profiles. *Proc. Natl Acad. Sci. USA* **102**, 15545–15550 (2005).
63. Polański, K. et al. Bin2cell reconstructs cells from high resolution Visium HD data. *Bioinformatics* **40**, btae546 (2024).
64. Cable, D. M. et al. Robust decomposition of cell type mixtures in spatial transcriptomics. *Nat. Biotechnol.* **40**, 517–526 (2022).
65. Singhal, V. et al. BANKSY unifies cell typing and tissue domain segmentation for scalable spatial omics data analysis. *Nat. Genet.* **56**, 431–441 (2024).
66. Arya, S., Mount, D. M., Netanyahu, N. S., Silverman, R. & Wu, A. Y. An optimal algorithm for approximate nearest neighbor searching fixed dimensions. *J. ACM* **45**, 891–923 (1998).
67. dos Santos Peixoto, R. et al. Characterizing cell-type spatial relationships across length scales in spatially resolved omics data. *Nat. Commun.* **16**, 350 (2025).
68. Zuccato, J. A. et al. Cerebrospinal fluid methylome-based liquid biopsies for accurate malignant brain neoplasm classification. *Neuro. Oncol.* **25**, 1452–1460 (2023).
69. Martin, M. Cutadapt removes adapter sequences from high-throughput sequencing reads. *EMBnet. J.* **17**, 10 (2011).
70. Langmead, B. & Salzberg, S. L. Fast gapped-read alignment with Bowtie 2. *Nat. Methods* **9**, 357–359 (2012).
71. Li, H. et al. The Sequence Alignment/Map format and SAMtools. *Bioinformatics* **25**, 2078–2079 (2009).
72. Lienhard, M., Grimm, C., Morkel, M., Herwig, R. & Chavez, L. MEDIPS: genome-wide differential coverage analysis of sequencing data derived from DNA enrichment experiments. *Bioinformatics* **30**, 284–286 (2014).
73. Leek, A. J. T. et al. Package sva: surrogate variable analysis. https://bioconductor.org/packages/release/bioc/html/sva.html (2018).
74. Ritchie, M. E. et al. limma powers differential expression analyses for RNA-sequencing and microarray studies. *Nucleic Acids Res.* **43**, e47 (2015).
75. Korotkevich, G. et al. Fast gene set enrichment analysis. Preprint at *bioRxiv* https://doi.org/10.1101/060012 (2016).
76. Zadeh, G. & Landry, A. Single cell meningioma [Data set]. *Zenodo*. https://doi.org/10.5281/zenodo.17874195 (2025).

Acknowledgements

We thank members of the International Consortium on Meningiomas for ongoing collaboration and discussions. We thank T. Tung from our laboratory for help with sample procurement, as well as J. Tsao, F. Aboualizadeh, T. Ketela and all the staff of the Princess Margaret Genomics Centre (https://pmgenomics.ca) for their expertise in generating some of the sequencing data used in this study.

Author contributions

A.P.L wrote and revised the manuscript and performed data analysis and figure preparation. J.L., V.P. and L.S.Y. performed additional analysis and data processing. A.P.L., L.S.Y. and J.Z.W. conducted sample collection and processing. A.P.L., L.S.Y., J.Z.W., A.A., C.G., Y.E., C.Q.D., Q.W., S.M. and O.S. performed genomic extraction, quantification and processing. A.A.C.-G. provided a subset of meningioma samples and metadata. A.G. and K.A. performed pathologic review. D.S.T. provided radiotherapy data of institutional retrospective meningioma cases. A.P.L., F.N. and G.Z. were responsible for study design and conception. All authors reviewed the manuscript and agreed with its submission.

Funding

Funding sources for this study include the Canadian Institutes of Health Research (CIHR) Project Fund (RN482811-481519 to G.Z., F.N. and J.Z.W.; PJT 206207 to G.Z., F.N. and A.P.L.), Brain Tumour Charity United Kingdom (GN-000693 to G.Z. and F.N.; GN-000790 to G.Z., F.N. and A.P.L.), the Terry Fox Research Institute (1144-03 to F.N.), the V Foundation for Cancer Research (G.Z.), the Iranian Canadian Pioneers Professorship in Neuro-Oncology (F.N.) and the Hold'em for Life Early Career Professorship in Cancer Research (F.N.).

Competing interests

The authors declare no competing interests.

Additional information

Extended data is available for this paper at https://doi.org/10.1038/s41588-026-02615-w.

Supplementary information The online version contains supplementary material available at https://doi.org/10.1038/s41588-026-02615-w.

Correspondence and requests for materials should be addressed to Farshad Nassiri or Gelareh Zadeh.

Peer review information *Nature Genetics* thanks Calixto-Hope Lucas, Jason Sa and the other, anonymous, reviewer(s) for their contribution to the peer review of this work. Peer reviewer reports are available.

https://doi.org/10.1038/s41588-026-02615-w

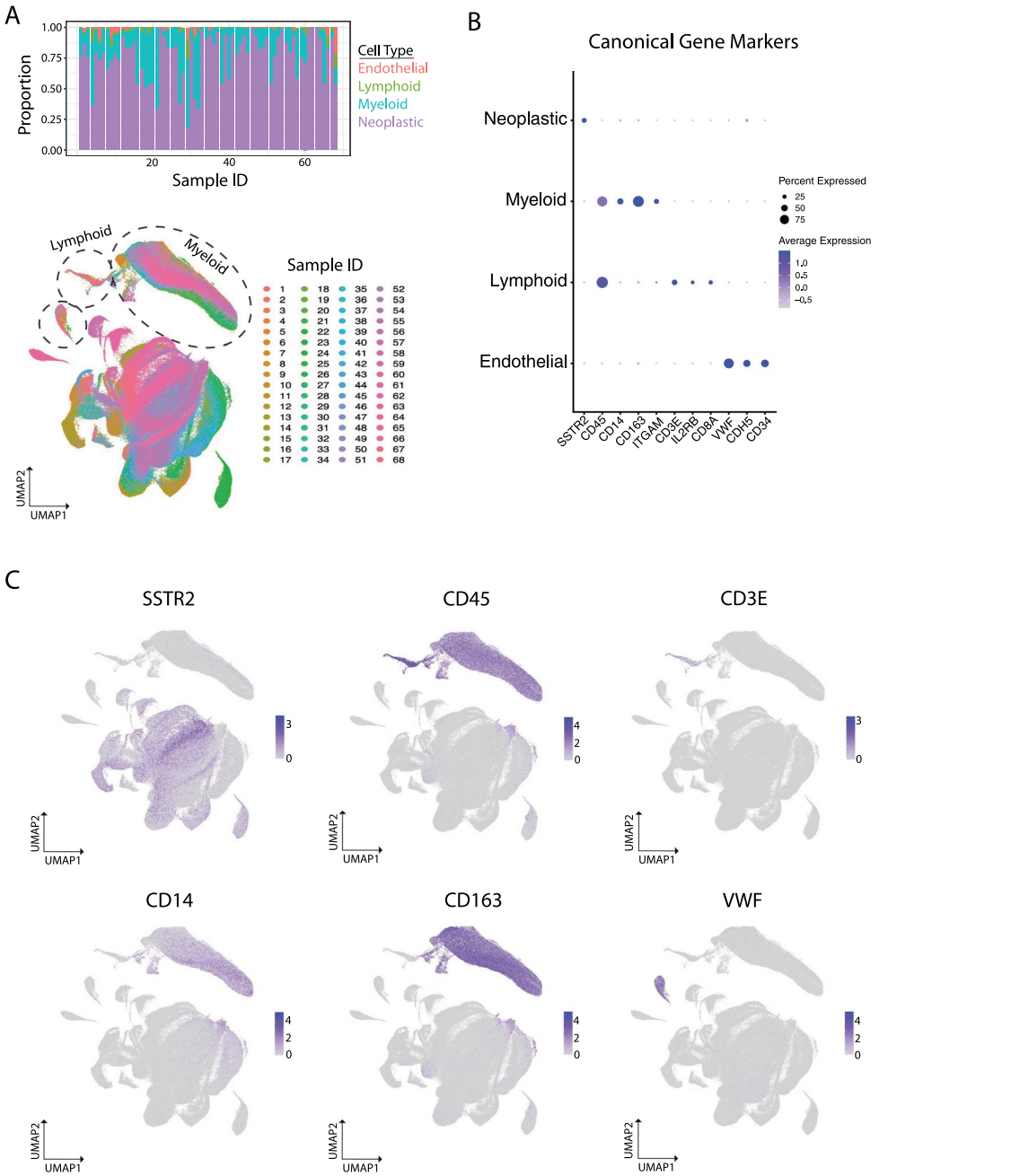

Extended Data Fig. 1 | Validation of cell type assignments. a) UMAP of all samples in our 'atlas' cohort, with each cell labeled based on patient of origin (bottom). Stacked barplot of cell proportions for each sample (top). **b**) Dotplot demonstrating expected upregulation of select canonical marker genes in their respective cell populations. **c**) Expression of select canonical marker genes in each cell within the same UMAP as in (A).

https://doi.org/10.1038/s41588-026-02615-w

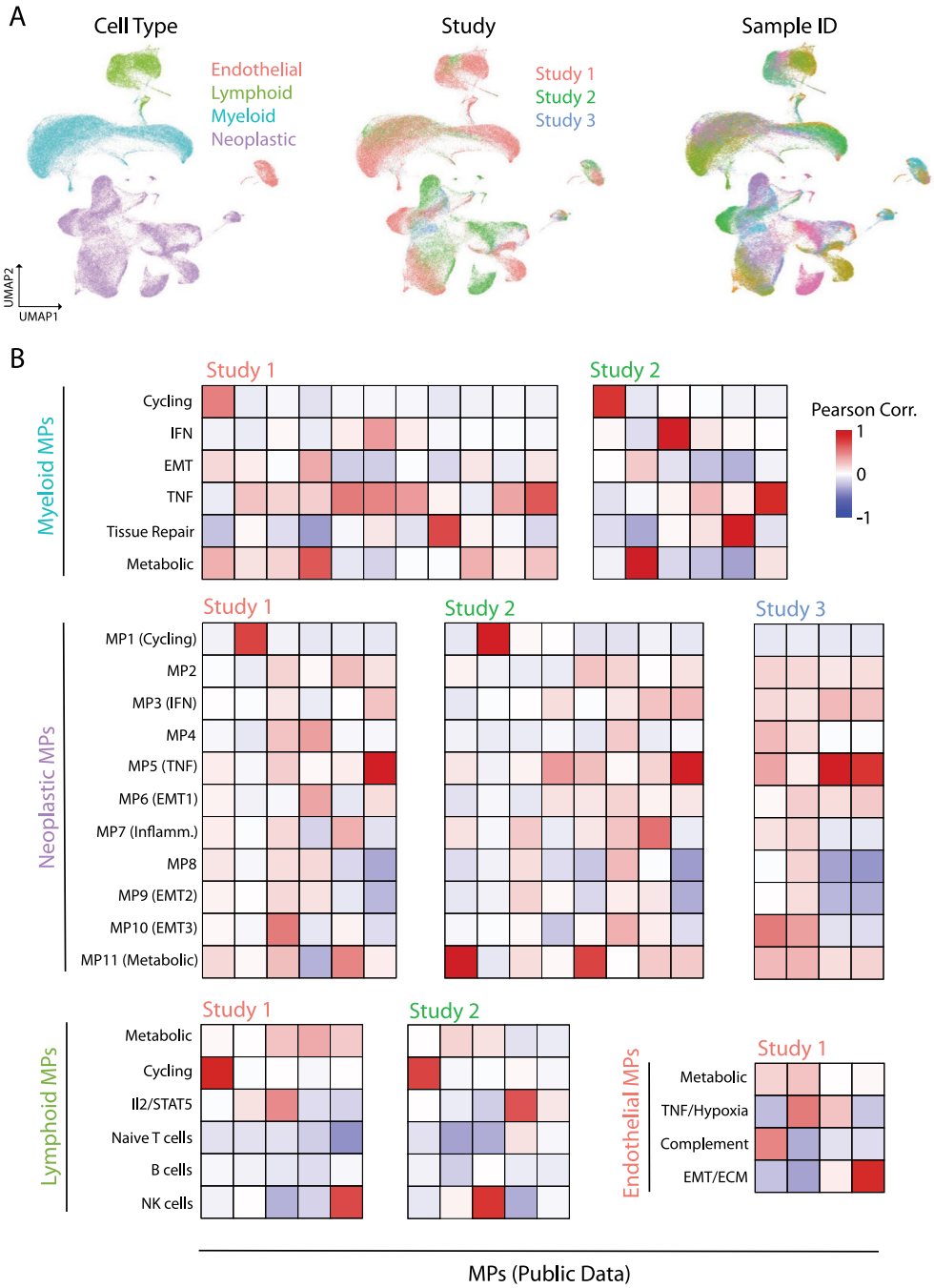

Extended Data Fig. 2 | Validation of cell states using publicly available data. **a**) UMAPs of all cells from 3 publicly available cohorts, batch-corrected by study and labeled by cell type (left), cohort (middle), and sample (right, with each color corresponding to a unique sample ID). Study 1 corresponds to GSE206647, study 2 corresponds to GSE278452, and study 3 corresponds to https://doi.org/10.5281/zenodo.4932158. **b**) Heatmaps depicting Pearson correlation values between metaprograms derived from our atlas cohort (rows) and those derived from publicly available data using the same approach. Metaprograms were computed from each public cohort individually to avoid batch effects. Within a particular cell type, samples were excluded if less than 50 cells were present, and a minimum of 4 samples per cohort were needed to proceed with metaprogram discovery. Numeric values of the most correlated metaprograms are plotted where the value is at minimum 0.4. MP = metaprogram.

https://doi.org/10.1038/s41588-026-02615-w

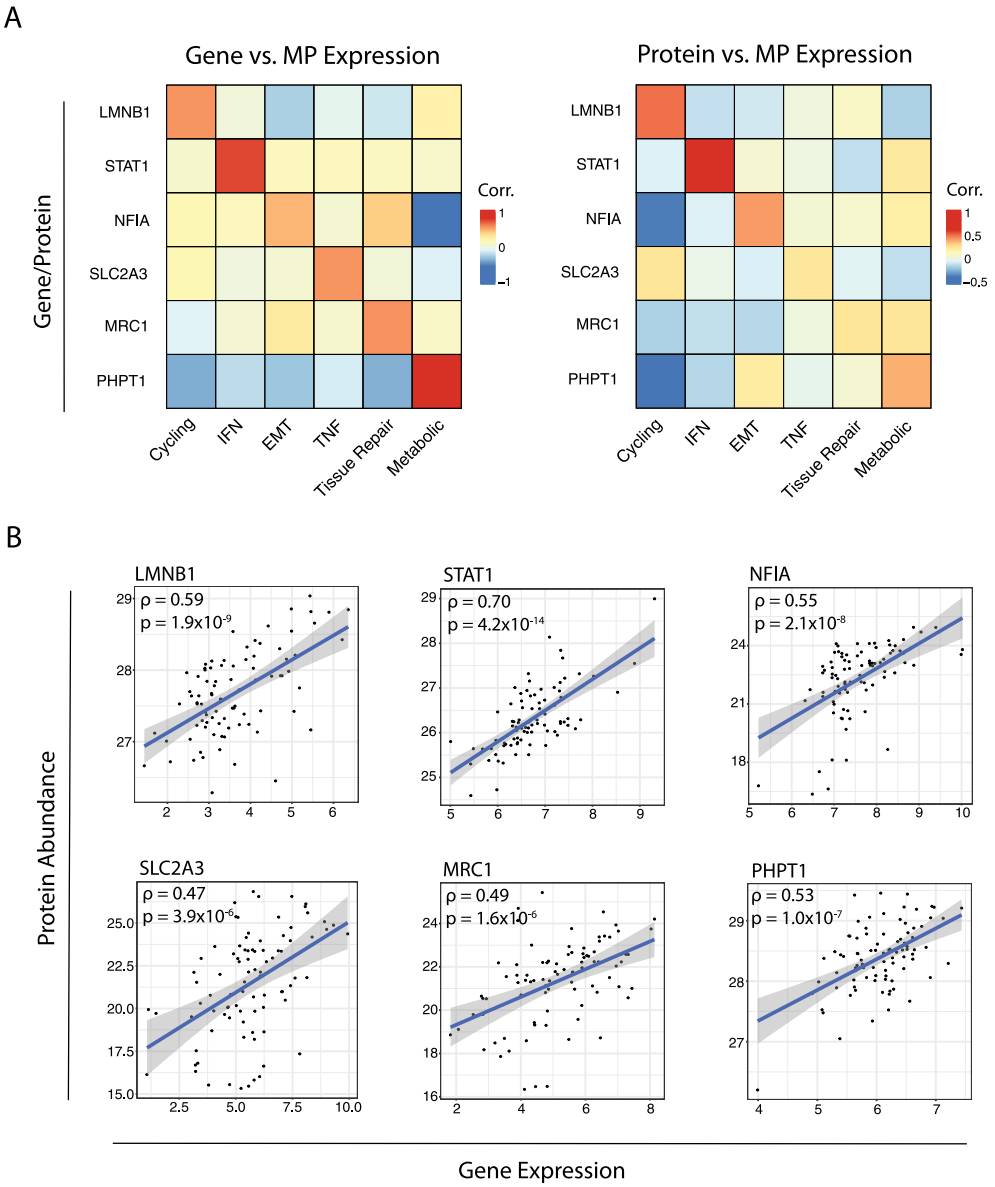

Extended Data Fig. 3 | Identifying individual protein/gene pairs which correlate with myeloid MP expression. a) Heatmaps depicting Pearson correlation values between expression of selected marker genes in bulk RNA sequencing data and expression of inferred myeloid metaprograms from the same bulk RNA data (left n = 712) and Pearson correlation values between the abundance of these same proteins and the inferred myeloid metaprogram expression on the subset of cases with matched proteomics (n = 88). **b**) Scatterplots depicting the relationship between the expression of each selected marker gene (bulk RNA sequencing) and its corresponding protein abundance on cases with both data available (n = 88). Fitted linear regression lines, Pearson correlation values, and two-sided p-values are shown, with the shaded area corresponding to the 95% confidence interval of the regression line. MP = metaprogram.

https://doi.org/10.1038/s41588-026-02615-w

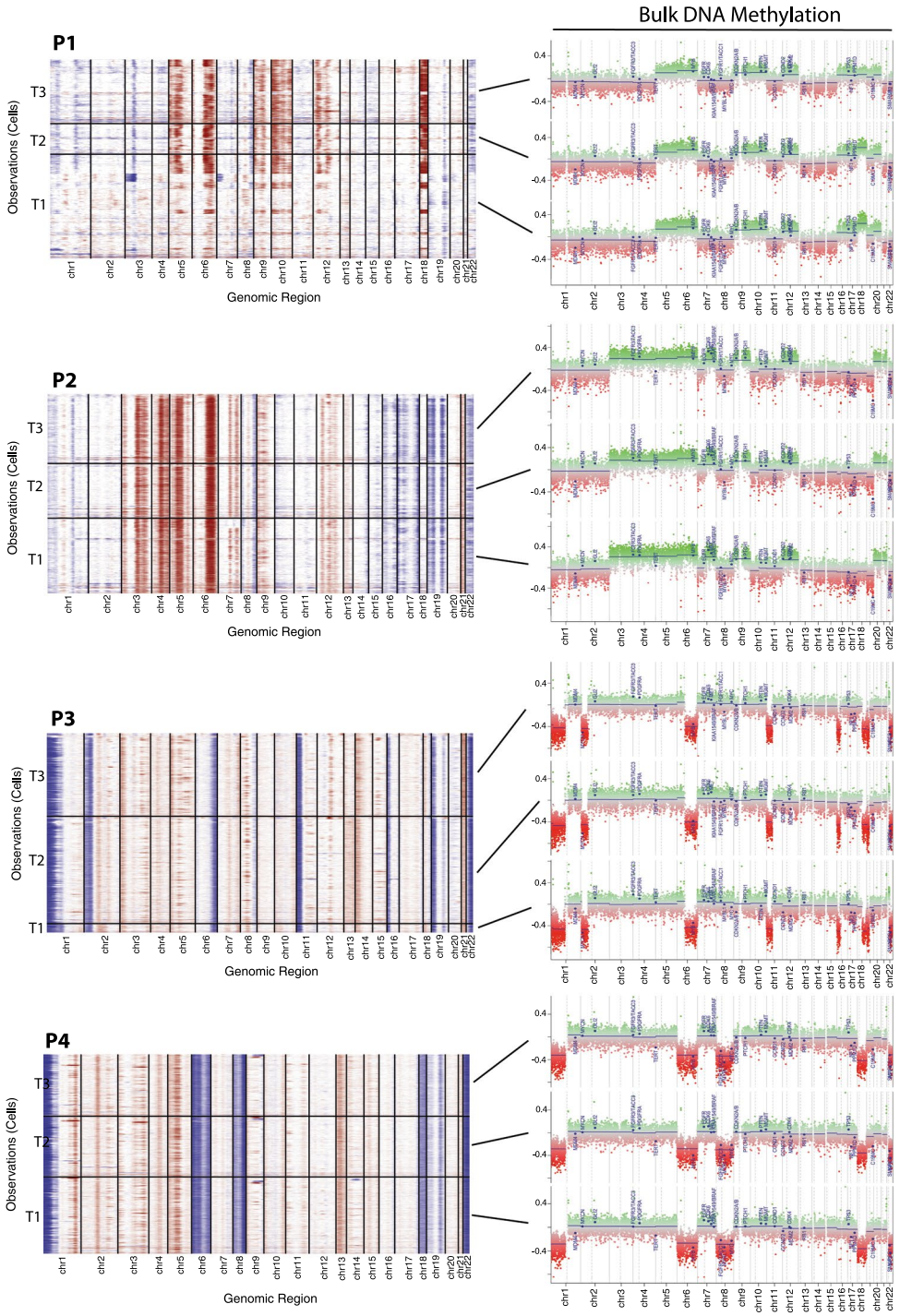

Extended Data Fig. 4 | Copy number alterations are consistent between bulk methylation and snRNA-seq. Inferred chromosomal copy number profiles by single nuclear RNA (left) and bulk DNA methylation (right) for each sample of the internal regional cohort. For the single-nuclear RNA sequencing (InferCNV), only neoplastic cells are included.

https://doi.org/10.1038/s41588-026-02615-w

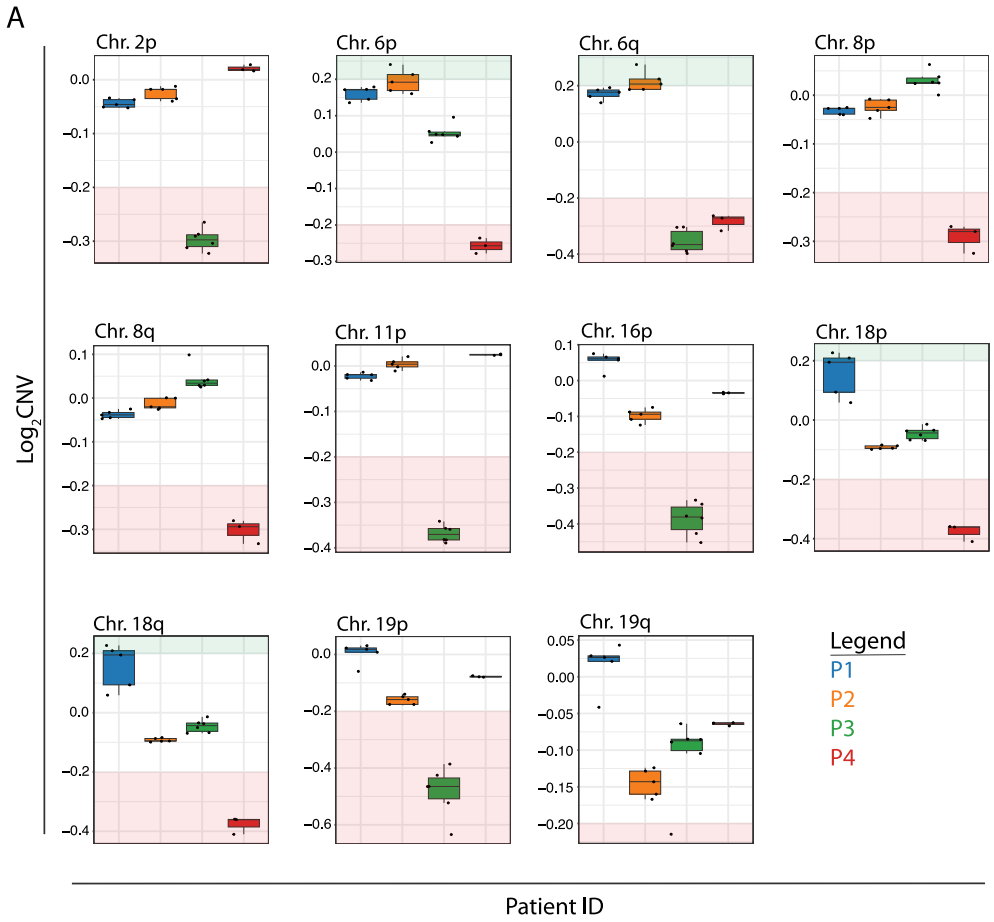

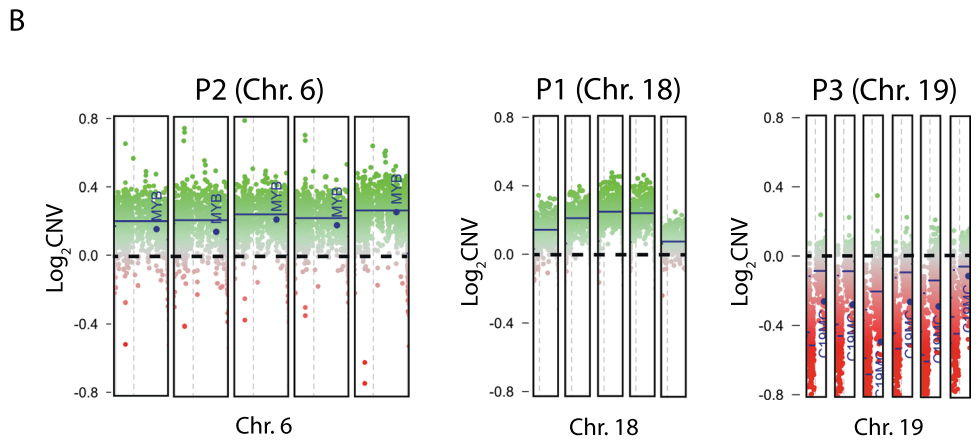

Extended Data Fig. 5 | DNA methylation-based CNV analysis reveals intra-tumoral stability of chromosome arm gains and losses. a) Boxplots of median log2CNV [copy number variation] values for each sample stratified by patient of origin for all chromosome arms with at least one sample having a defined loss (log2CNV < -0.2, highlighted in red) or gain (log2CNV > 0.2, highlighted in green). Center lines represent median and the box spans the interquartile range; whiskers extend to the most extreme values within 1.5 times the interquartile range beyond the quartiles. There are 5 samples for P1, 5 samples for P2, 6 samples for P3, and 3 samples for P4. **b**) CNV plots of cases where there is inconsistent labeling of a gain or loss across samples from the same patient based on this threshold.

https://doi.org/10.1038/s41588-026-02615-w

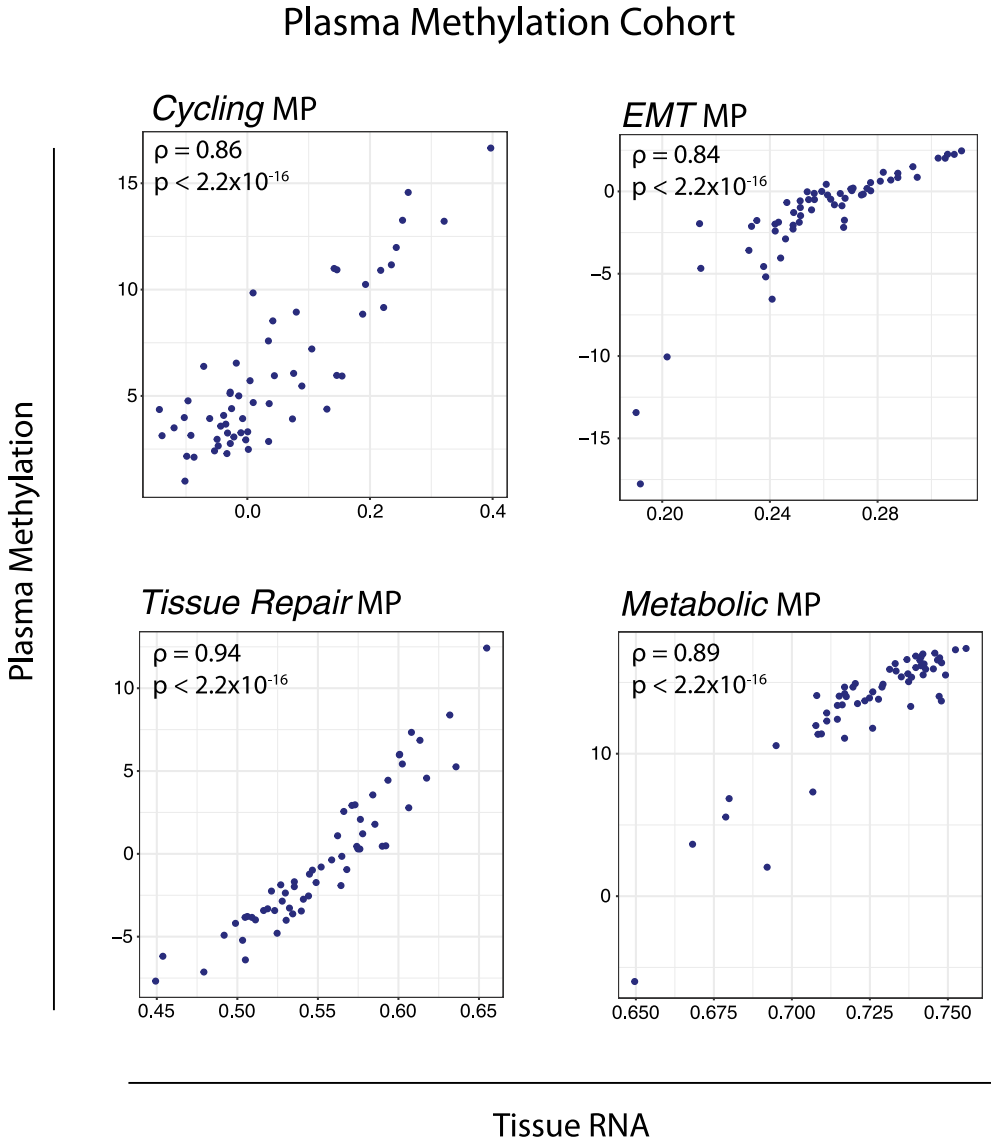

Extended Data Fig. 6 | Plasma methylation may be useful at identifying myeloid MPs noninvasively. Scatterplots of the tissue RNA-based myeloid state expression (x-axis) vs. the plasma methylation signatures of these metaprograms among the subset of cases with plasma methylation data available (n = 59). Pearson correlation values and corresponding 2-sided p-values are shown. MP = metaprogram.

nature portfolio

Corresponding author(s): Zadeh, Gelareh
Nassiri, Farshad

Last updated by author(s): April 9, 2026

Reporting Summary

Nature Portfolio wishes to improve the reproducibility of the work that we publish. This form provides structure for consistency and transparency in reporting. For further information on Nature Portfolio policies, see our Editorial Policies and the Editorial Policy Checklist.

Statistics

For all statistical analyses, confirm that the following items are present in the figure legend, table legend, main text, or Methods section.

n/a	Confirmed
☐	☒ The exact sample size (*n*) for each experimental group/condition, given as a discrete number and unit of measurement
☐	☒ A statement on whether measurements were taken from distinct samples or whether the same sample was measured repeatedly
☐	☒ The statistical test(s) used AND whether they are one- or two-sided *Only common tests should be described solely by name; describe more complex techniques in the Methods section.*
☐	☒ A description of all covariates tested
☐	☒ A description of any assumptions or corrections, such as tests of normality and adjustment for multiple comparisons
☐	☒ A full description of the statistical parameters including central tendency (e.g. means) or other basic estimates (e.g. regression coefficient) AND variation (e.g. standard deviation) or associated estimates of uncertainty (e.g. confidence intervals)
☐	☒ For null hypothesis testing, the test statistic (e.g. *F*, *t*, *r*) with confidence intervals, effect sizes, degrees of freedom and *P* value noted *Give P values as exact values whenever suitable.*
☒	☐ For Bayesian analysis, information on the choice of priors and Markov chain Monte Carlo settings
☒	☐ For hierarchical and complex designs, identification of the appropriate level for tests and full reporting of outcomes
☐	☒ Estimates of effect sizes (e.g. Cohen's *d*, Pearson's *r*), indicating how they were calculated

Our web collection on statistics for biologists contains articles on many of the points above.

Software and code

Policy information about availability of computer code

Data collection	No specific software was used.
Data analysis	All data analyses were performed in R and Python. The following publicly available tools were used for analyses: BayesPrism (v2.2.2), survival (v3.6.4), survminer (v0.4.9), GSVA (v1.52.3), edgeR (v4.2.1), CellChat (v2.1.2), Seurat (v5.1.0), patchwork (v1.2.0), NMF (v0.28), monocle3 (v1.3.7), scATOMIC (v2.0.3), scDblFinder (v1.18.0), AUCell (v1.26.0), Banksy (v1.1.0), spacexr (v2.2.1), distances (v0.1.11), scCustomize (v3.0.1), bin2cell (v0.3.3), CellNEST, conumee (v1.38.0), minfi (v1.50.0), Celda (v1.20.0), DIEM (v2.4.1), infercnv (v1.20.0), Trim Galore (v0.5.0), STAR aligner (v2.7.9a), FNN (v1.1.4), RANN (v2.6.1), crawdad (v1.0.1), spatstat (v3.3-0), sva (v3.52.0), fgsea (v1.30.0), HTSeq (v0.11.0), cutadapt (v2.5), fastQC (v0.11.5), Bowtie2 (v2.3.5), Samtools (v1.20), MEDIPS (v1.56.0).

For manuscripts utilizing custom algorithms or software that are central to the research but not yet described in published literature, software must be made available to editors and reviewers. We strongly encourage code deposition in a community repository (e.g. GitHub). See the Nature Portfolio guidelines for submitting code & software for further information.

Data

Policy information about availability of data

All manuscripts must include a data availability statement. This statement should provide the following information, where applicable:

- Accession codes, unique identifiers, or web links for publicly available datasets
- A description of any restrictions on data availability
- For clinical datasets or third party data, please ensure that the statement adheres to our policy

All code generated as part of this work has been deposited to Zenodo at URL 10.5281/zenodo.17874195.
Newly generated raw sequencing data (fastq files) and associated clinical metadata have been deposited at the European Genome-Phenome Archive (https://ega-archive.org/: EGAD50000002214 for cfMeDIP-seq data, EGAD50000002233 for Visium HD data, and EGAD50000002272 for snRNAseq data). Publicly-available single-cell resolution RNA sequencing data was obtained from GSE206647, GSE278452, and https://doi.org/10.5281/zenodo.4932158. Proteomic data was deposited as part of a prior publication to the Mass Spectrometry Interactive Virtual Environment (MassIVE, ID MSV000086901). Bulk DNA methylation (IDAT files) and RNA sequencing (fastq files) data have been deposited from previous publications (https://www.ncbi.nlm.nih.gov/geo/: GSE180061, GSE270371, https://ega-archive.org/: EGAS0001004982,
https://www.ncbi.nlm.nih.gov/sra: PRJNA1127224,database of Genotypes and Phenotypes (dbGaP), phs003707.v1.p1), or was obtained from publicly available cohorts (GSE189521, GSE183656).

Research involving human participants, their data, or biological material

Policy information about studies with human participants or human data. See also policy information about sex, gender (identity/presentation), and sexual orientation and race, ethnicity and racism.

Reporting on sex and gender	All patients with available samples were included in this study with no recruitment bias based on sex or gender.
Reporting on race, ethnicity, or other socially relevant groupings	All patients with available samples were included in this study with no recruitment bias based on race, ethnicity, or other social groupings.
Population characteristics	Within our large clinical cohort of patients with bulk mRNA sequencing data (n = 712), the median age was 57 (IQR 47.5-66.5) years. A total of 484/710 patients (68.2%) were female, which is consistent with the reported epidemiology of meningioma.
Recruitment	Eligible cases were patients with pathologically confirmed meningioma with samples available from institutional biobanks. Participants were consented for institutional biobanking for research at the time of surgery.
Ethics oversight	This study was approved by the Institutional Review Board at University Health Network

Note that full information on the approval of the study protocol must also be provided in the manuscript.

Field-specific reporting

Please select the one below that is the best fit for your research. If you are not sure, read the appropriate sections before making your selection.

☒ Life sciences ☐ Behavioural & social sciences ☐ Ecological, evolutionary & environmental sciences

For a reference copy of the document with all sections, see nature.com/documents/nr-reporting-summary-flat.pdf

Life sciences study design

All studies must disclose on these points even when the disclosure is negative.

Sample size	Sample selection was based on availability of tissue and clinical data, and feasibility for the collection of prospective samples with dedicated multi-regional profiling. Sample numbers were sufficient for the analyses performed.
Data exclusions	No samples were unexpectedly excluded from our analysis
Replication	Sequencing and molecular profiling was performed once per human sample because of the limited amount of tissue that is available per patient.
Randomization	N/A
Blinding	Samples were blinded to clinical data during sample preprocessing and sequencing

Reporting for specific materials, systems and methods

We require information from authors about some types of materials, experimental systems and methods used in many studies. Here, indicate whether each material, system or method listed is relevant to your study. If you are not sure if a list item applies to your research, read the appropriate section before selecting a response.

Materials & experimental systems

n/a	Involved in the study
☒	☐ Antibodies
☒	☐ Eukaryotic cell lines
☒	☐ Palaeontology and archaeology
☒	☐ Animals and other organisms
☒	☐ Clinical data
☒	☐ Dual use research of concern
☒	☐ Plants

Methods

n/a	Involved in the study
☒	☐ ChIP-seq
☒	☐ Flow cytometry
☒	☐ MRI-based neuroimaging

Plants

Seed stocks	N/A
Novel plant genotypes	N/A
Authentication	N/A